Theoretico-experimental analysis of bistability in the oscillatory response of a TaOx ReRAM to

frontiers | Frontiers in Nanotechnology

TYPE Original Research
PUBLISHED 15 May 2024
DOI 10.3389/fnano.2024.1301320

OPEN ACCESS

EDITED BY
Carlo Ricciardi,
Polytechnic University of Turin, Italy

REVIEWED BY
Alberto Tesi,
University of Florence, Italy
Christos Papavassiliou,
Imperial College London, United Kingdom

*CORRESPONDENCE
A. Ascoli,
alon.ascoli@polito.it

RECEIVED 24 September 2023
ACCEPTED 19 March 2024
PUBLISHED 15 May 2024

CITATION
Schmitt N, Ascoli A, Messaris I, Demirkol AS, Menzel S, Rana V, Tetzlaff R and Chua LO (2024), Theoretico-experimental analysis of bistability in the oscillatory response of a TaO_x ReRAM to pulse train stimuli.
Front. Nanotechnol. 6:1301320.
doi: 10.3389/fnano.2024.1301320

Theoretico-experimental analysis of bistability in the oscillatory response of a TaO_x ReRAM to pulse train stimuli

N. Schmitt[1], A. Ascoli[2]*, I. Messaris[1], A. S. Demirkol[1], S. Menzel[3], V. Rana[4], R. Tetzlaff[1] and L. O. Chua[5]

[1]Institute of Circuits and Systems, Faculty of Electrical and Computer Engineering, Technische Universität Dresden, Dresden, Germany, [2]Department of Electronics and Telecommunications, Politecnico di Torino, Turin, Italy, [3]Peter Grünberg Institut 7, Forschungszentrum Jülich GmbH, Jülich, Germany, [4]Peter Grünberg Institut 10, Forschungszentrum Jülich GmbH, Jülich, Germany, [5]Department of Electrical Engineering and Computer Sciences, University of California, Berkeley, Berkeley, CA, United States

Fading memory is the capability of a physical system to approach a unique asymptotic behaviour, irrespective of the initial conditions, when stimulated by an input from a certain class. Standard stimuli from the AC periodic class typically induce fading memory effects in non-volatile memristors, as uncovered for the first time back in 2016. Very recently, a deep investigation of resistance switching phenomena in a TaO_x resistive random access memory cell revealed the capability of the nano-device to exhibit one of two possible oscillatory behaviours, depending upon the initial condition, when subject to a particular periodic excitation. This interesting finding was, however, left unexplained. Bistability is the simplest form of local fading memory. In a system, endowed with local fading memory under a given stimulus, the initial condition does not affect the long-term behaviour of the state as long as it is drawn from the basin of attraction of either of the distinct coexisting state-space attractors (two limit cycles for the periodically forced memristor acting as a bistable oscillator). Here, the history of the system, encoded in the initial condition, is, thus, erasable only locally through *ad hoc* stimulation. Motivated by the discovery of local history erase effects in our resistive random access memory cell, this study applies a powerful system-theoretic tool, enabling the analysis of the response of first-order systems to square pulse train-based periodic stimuli, known as the time-average state dynamic route, to an accurate physics-based mathematical model, earlier fitted to the nano-device, to determine a strategy for specifying the parameters of an excitation signal, consisting of the sequence of two square pulses of opposite polarity per period so as to induce various forms of monostability or multistability in the non-volatile memristor. In particular, as an absolute novelty in the literature, experimental measurements validate the theoretical prediction on the capability of the device to operate as one of two distinct oscillators, depending upon the initial condition, under a specific pulse train excitation signal. The coexistence of multiple oscillatory operating modes in the periodically forced resistive

random access memory cell, an example par excellence of their unique non-linear dynamics, may inspire the development and circuit implementation of novel sensing and mem-computing paradigms.

KEYWORDS

ReRAM, non-volatility, fading memory, local fading memory, bistability, tristability, multistability, time-average state dynamic route

1 Introduction

Resistance switching memories (Ielmini and Waser, 2016), falling in the class of non-volatile memristors (Chua, 2018), are currently under the zooming lens of thousands of researchers worldwide (Buckwell et al., 2021; Shamsi et al., 2021; Milano et al., 2022; Lenk et al., 2023; Tzouvadaki et al., 2023) for the wide spectrum of opportunities they open up in the post-Moore electronics era (Yi et al., 2022). In addition to their obvious use as *data storage* units, memristors from the non-volatile class (Mikolajick et al., 2009; Vontobel et al., 2009) may be alternatively operated as data processing elements, enabling the circuit implementation of innovative *in-memory computing* paradigms (Xia and Yang, 2019), which promise to resolve the von Neumann bottleneck, limiting the performance of state-of-the-art computers, in which the central processing unit is frequently forced to remain in an idle state, preventing its potential to be fully harnessed, to enable relevant data transfer across the physical channel, which allows its communication with the physically separated memory. Furthermore, their typical arrangement within dense crossbar arrays, whose design exploits the need to introduce thin oxide films for isolation purposes between adjacent metal layers in standard CMOS fabrication processes, favours the development of hardware engines, which leverage state-dependent Ohm's law-based electronic transport in the nano-device to *accelerate matrix-vector multiplications* (Hu et al., 2016), lying at the core of most machine learning algorithms for Big Data analysis nowadays. Despite the considerable progress, achieved over the past 15 years through the pursuit of significant research studies (Waser and Aono, 2007; Valov et al., 2013; Wang et al., 2017; Rao et al., 2023) aimed to understand the fundamentals of the operating mechanisms of resistance switching memories, some aspects of the intricate, yet peculiar, non-linear dynamics (Corinto et al., 2015) of these devices, of potential interest for electronic applications (Talati et al., 2016; Sebastian et al., 2017; Di Ventra and Traversa, 2018; Li et al., 2018; Zidan et al., 2018), are yet to be discovered. Back in 2016, the theoretical analysis of a predictive mathematical model by Strachan et al. (2013) first unveiled the emergence of *memory loss phenomena* (Ascoli et al., 2017), coexisting with analogue non-volatility, in a TaO_x resistive random access memory (ReRAM) device under suitable periodic excitation. As confirmed shortly later in laboratory measurements, carried out on a physical sample at Hewlett Packard Labs (Ascoli et al., 2016c), the initial condition was found to have no impact on the asymptotic oscillatory behaviour of the periodically driven non-volatile memory device. History erase effects were found to appear across this memristor physical realization under a wide class of periodic stimuli, typically employed in electrical engineering, including triangular, square, and sine waves. The ubiquity of this non-linear dynamic phenomenon in non-volatile memristors was further revealed shortly later (Menzel et al., 2017; Ascoli et al., 2018). The fading memory phenomenon originates in real non-volatile memristor devices due to the intrinsic asymmetry in their SET and RESET switching kinetics. In fact, constructing artificially a device model with symmetric ON and OFF dynamics, as is the case for ideal memristors, no history erase effect would be observed, irrespective of the stimulus. In these circumstances, the periodically forced device would be found to exhibit an initial condition-dependent oscillatory behaviour directly from the beginning of the AC stress test. On the other hand, in general, a physical memristor realisation, under periodic excitation, undergoes transient phenomena, before locking into some oscillatory operating mode, whereby the effect of SET and RESET forces on its kinetics balances out over each input cycle. In system theory, a physical system, which exhibits a unique asymptotic behaviour under a given stimulus, is said to have *fading memory* (Boyd and Chua, 1985) on that stimulus. A local form of fading memory was introduced theoretically in Ascoli et al. (2016a) to define the capability of a physical system to lock into one of a number of distinct operating modes under a given excitation, depending upon the initial condition. A physical system of this kind is said to undergo fading memory effects locally within the basin of attraction of each of the locally stable attractors in the associated state space. Although a memristive circuit, employing standard electrical components, including active components, was designed in Ascoli et al. (2016b) to provide a pedagogical example of a physical system, endowed with *local fading memory* on a given input class, no physical memristor realisation was ever found to experience *input-induced multistability* until recent observations of bistability in the oscillatory behaviour of the state of the Strachan model under suitable pulse train-based excitation, as reported in an interesting bifurcation study from Pershin and Slipko (2019). A comprehensive theoretico-experimental research study (Ascoli et al., 2022), allowing to gain a deep insight into the mechanisms, underlying resistance switching phenomena in another ReRAM cell—composed of a $Ta/TaO_x/Pt$ device stack—and manufactured at the premises of Forschungszentrum Jlich (FZJ), similarly reported the coexistence of two stable oscillatory solutions for the dimensionless memory state x of the associated physics-based mathematical description (Hardtdegen et al., 2018), known as the Jülich Aachen resistive switching tool (JART) valence change memory (VCM) model (Bengel et al., 2022), preliminarily fitted to experimental data, extracted from a device sample, under a particular symmetric periodic triangular stimulus. The device

was found to operate around its fully-RESET state in one of the two oscillatory operating modes. The research work, presented in this manuscript, intends to answer key questions, which emerged from this observation, as listed here.

1. Is it possible to elucidate the mechanisms behind the emergence of bistability in the oscillatory response of our ReRAM cell under suitable periodic stimulation, as reported yet left unexplained in Ascoli et al. (2022)?
2. Is it possible to excite the nano-device in such a way that it may feature a larger number of coexisting oscillatory operating modes?
3. Is it possible to modulate the excitation signal in such a way to switch the nature of the device oscillatory response from unimodal to multimodal, or vice versa?
4. Is there a quantitative measure for identifying each possible asymptotic oscillatory steady state for the device, subject to a given periodic stimulus, from the analysis of the competition between the counteractive forces, acting on the device kinetics, under SET and RESET phases over each cycle?
5. Is it possible to develop a rigorous methodology to tailor the shape of the periodic stimulus in such a way to induce a variable number of stable oscillatory operating modes into the device?
6. Is it possible to demonstrate experimentally the emergence of the simplest form of local fading memory in a non-volatile memristor?

In order to address these points, a powerful system-theoretic graphic tool, known as the *time-average state dynamic route* (TA-SDR), inspired from the bifurcation study in Pershin and Slipko (2019), exploiting the *time-averaging method* from the theory of non-linear dynamics (Guckenheimer and Holmes, 1983), is applied to the JART VCM model to derive a systematic technique for massaging the properties of two square pulses of opposite polarity, composing the train-based stimulus over each cycle, for inducing monostability or multistability in the oscillatory response of the TaO_x ReRAM nano-device manufactured in house. For one particular input parameter setting, the predictions from the proposed theory are validated experimentally in our laboratory facilities, strengthening the significance of our research findings. In regard to the structure of this paper, the motivation behind our research work is elucidated in Section 2. The TA-SDR technique, extending the dynamic route map (DRM) concept (Chua, 2018) to enable the analysis of the time evolution of the mean value of the memory state of a first-order dynamical system under square pulse train stimulation, in those circumstances where the memory state undergoes small changes per cycle, which is the case, for example, in high-frequency excitation scenarios (Messaris et al., 2023), is introduced in Section 3. Section 4 presents a rigorous methodology, based upon the TA-SDR tool, allowing to determine appropriate heights and widths for the two pulses, composing the train stimulus over each cycle so as to endow the time-average state equation (TA-SE), governing the dynamics of the mean value $\bar{x}$ of the dimensionless memory state x of the ReRAM cell under the given periodic excitation, with a desired number of stable equilibria, which correspond to the levels around which the dimensionless memory state itself would be found to revolve at a steady state, upon choosing initial conditions from the basin of attraction of the corresponding periodic attractor (Schmitt et al., 2023). Section 5 provides pedagogical examples, demonstrating the accuracy of the proposed methodology, applied to the JART VCM model, reviewed in Supplementary Appendix A.1, to guide the circuit designer toward a robust choice for the input parameters to induce the coexistence of a desired number of stable oscillatory solutions for the device memory state. Section 6 explores other regions of the two-dimensional pulse height parameter space, identifying novel multimodal steady-state oscillatory dynamics for the ReRAM cell upon suitable pulse width ratio modulation, while taking care for the physical limitations of the measurement tools, available to us so as to set the ground for experimental multistability tests on the oscillatory device. The study in this section inspired the identification of a suitable input parameter setting, which, programmed in a physical pulse source generator, was found to induce a bistable oscillatory response in a VCM device sample, as observed experimentally for the first time ever in the laboratory, confirming the validity of the theoretical predictions (refer to Section 7). Moreover, Supplementary Appendix A.2 describes the promising outcome of preliminary activities aimed to specify train stimulus properties, which comply with the limited capabilities of the pulse generators in consideration, and enable endowing the ReRAM cell with three oscillatory operating modes, two of which, envisaging resistance excursions, well-confined within the allowable range. As reported in the conclusions, drafted in Section 8, the capability of a ReRAM cell to admit coexisting oscillatory modes under suitable periodic stimulation could be leveraged in novel circuits for sensing, processing, and storing data more efficiently than what is currently feasible in purely CMOS electrical systems.

2 Motivation

The TaO_x ReRAM cell, under focus in this research study, is a voltage-controlled VCM device. The voltage v (current i) across (through) its physical stack then acts as the input (output) variable for the associated memristor model. The differential algebraic equation (DAE) set of the JART VCM model, which captures very accurately the device dynamics and is the object of the theoretical analysis to follow, may be numerically cast, as explained in Supplementary Appendix A.1, in the characteristic form of a first-order voltage-controlled extended memristor, i.e.,

$$\frac{dx}{dt} = g(x, v), \tag{1}$$

$$i = G(x, v) \cdot v, \text{ with } \lim_{v \to 0} G(x, v) \neq \infty, \tag{2}$$

where the ordinary differential equation (ODE) (Eq. 1), known as the *state equation* (SE), governs the time evolution of a dimensionless memory state x, constrained to lie at all times within a closed set $\mathcal{D}_x = [x_{\min}, x_{\max}]$, in which $x_{\min}$ ($x_{\max}$) denotes the lowest (highest) admissible memory state value, while the algebraic relation (Eq. 2) defines a state- and input-dependent Ohm's law (OL). In the first (latter) of these two equations, $g(x, v)$ ($G(x, v)$) is referred to as the state evolution (memductance) function. Figure 1, visualising an observation similar to that reported in Ascoli

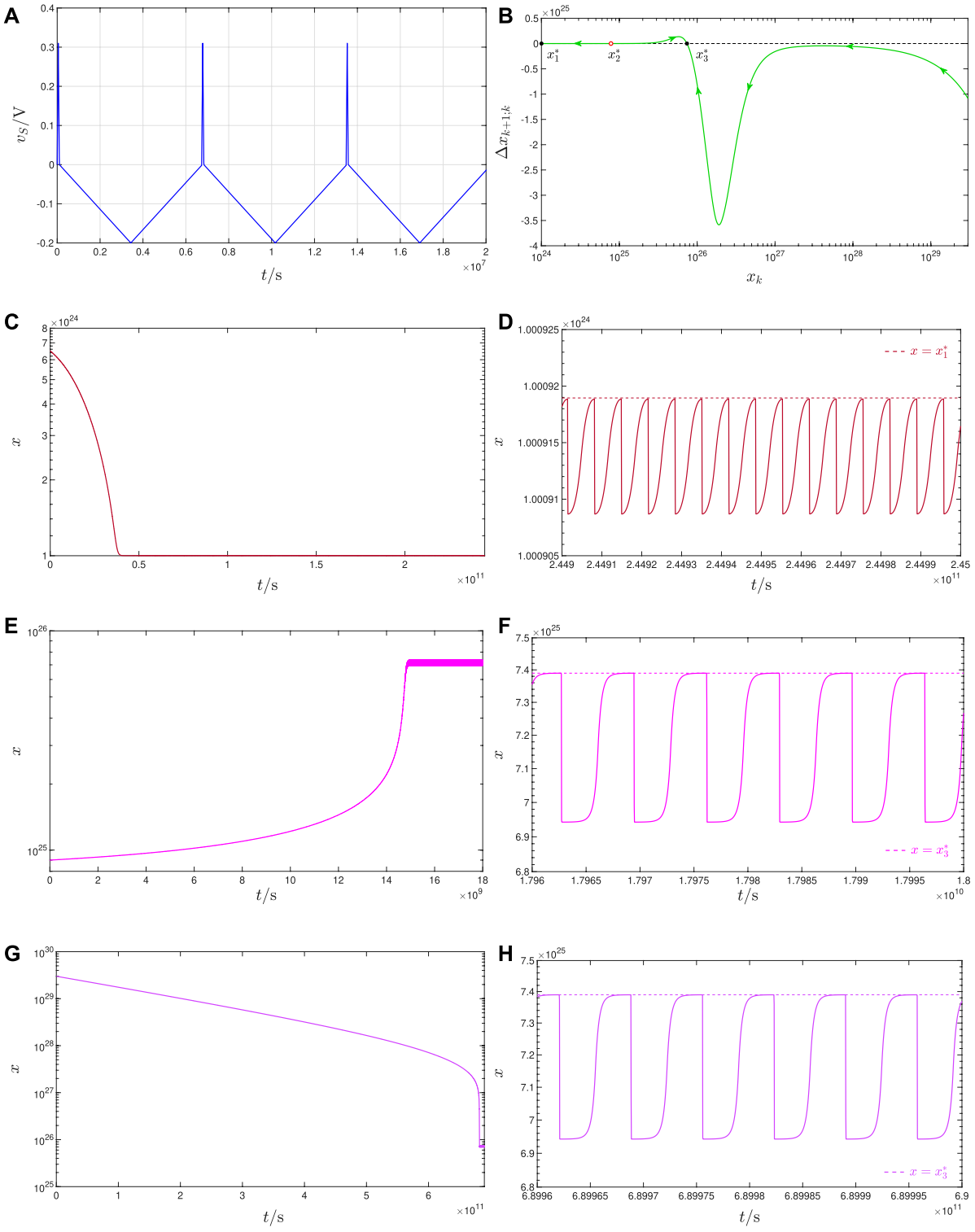

FIGURE 1
(A) Time waveform of an asymmetric periodic triangular voltage stimulus v_S, which, according to the JART VCM model predictions, induces bistable steady-state oscillatory dynamics in the TaO_x ReRAM cell, manufactured in Jülich, as it falls continuously between its terminals. The amplitude V_+ (V_-) and width τ_+ (τ_-) of the positive RESET (negative SET) triangular pulse over each input cycle are, respectively, set to 0.31 V (−0.2 V) and $1 \cdot 10^5$s ($6.6667 \cdot 10^6$s). The period T of the stimulus is then $\tau_+ + \tau_- = 6.7667 \cdot 10^6$s. The reset–set pulse width ratio $r \triangleq \tau_+/\tau_-$ amounts here to $1.5 \cdot 10^{-2}$. **(B)** $\Delta x_{k+1;k}$ *versus* x_k locus (Ascoli et al., 2023b), as extracted from the Poincaré map $x_{k+1} = \mathcal{P}(x_k)$ of the periodically forced ODE (Eq. 1) in the excitation scenario under examination. Here, the Poincaré map admits three fixed points, specifically $x_1^* = 1.000919 \cdot 10^{24}$, $x_2^* = 7.809066 \cdot 10^{24}$, and $x_3^* = 7.389705 \cdot 10^{25}$, of which each of the outer ones (the inner one) is asymptotically stable (is unstable), as indicated via a black filled (red hollow) circle marker. **(C, E, G)** [**(D, F, H)**]: Transients (steady state) in the time waveform of the numerical solution to the state Eq. 1 from the first, second, and third initial conditions x_0 in the set
(*Continued*)

FIGURE 1 (Continued)
$\{6.5 \cdot 10^{24}, 9 \cdot 10^{24}, 3 \cdot 10^{29}\}$. The JART VCM model is numerically integrated for as many as 36,818, 2,696, and 103,000 input cycles to allow its solution to attain the steady state in the first, second, and third simulations, respectively. Importantly, $x_1^{\prime}$ ($x_3^{\star}$) coincides with the maximum of the low-amplitude (large-amplitude) oscillation in the state, as shown in plot **(D)** [in either of plots **(F)** and **(H)**].

et al. (2022), illustrates how, depending upon the initial condition $x_0 \triangleq x\,(0)$, assigned to the dimensionless state x of the JART VCM model, the asymptotic oscillatory solution of the ODE (Eq. 1) may evolve along one of two distinct locally stable oscillatory waveforms, upon forcing the device voltage v to follow an asymmetric periodic voltage stimulus v_S, composed of a first-positive RESET[1] triangular pulse of amplitude $\hat{v}_{S,+} = +0.31$V, stretching across a time span $\tau_+ = 1 \cdot 10^5$s, and of a second-negative SET triangular pulse of amplitude $\hat{v}_{S,-} = -0.2$V, covering a time interval $\tau_- = 6.6667 \cdot 10^6$s, over each cycle of duration $T = \tau_+ + \tau_- = 6.7667 \cdot 10^6$s [refer to plot (a)], as established by the circuit setup of Figure 2A. Plot (b) depicts the graph of the state change per cycle map (SCPCM) (Ascoli et al., 2023b), which is dictated by the vector field of the non-autonomous[2] first-order ODE (Eq. 1) under the specified excitation scenario.

Remark 1. Let us consider a first-order ODE system, falling in the class (Eq. 1), where x is a scalar state with the existence domain $\mathcal{D}_x \triangleq (x_{\min}, x_{\max})$, while v denotes a particular periodic excitation signal v_S with T-long cycles. Let us denote the sample of the solution x of the periodically forced ODE at the end of the kth input cycle as $x_k \triangleq x(k \cdot T)$, for $k \in \mathbb{N}_0$. The SCPCM (Ascoli et al., 2023b) provides the change $\Delta x_{k+1;k} \triangleq x_{k+1} - x_k$, which the state x undergoes over the $(k+1)^{th}$ input cycle for each k-value in the set $\{0, 1, 2, \ldots\}$. The SCPCM can, thus, be easily retrieved from the one-dimensional discrete-time system $x_{k+1} = \mathcal{P}(x_k)$, referred to as Poincaré map[3] in non-linear dynamics theory (Guckenheimer and Holmes, 1983), computable from the list of values obtained by sampling the solution to the first-order ODE, subject to the specified periodic input signal $v = v_S$, at regular T-long time intervals. Assuming that the state sample x_k at the end of the kth input cycle satisfies the inequality $\mathcal{P}(x_k) > (<) x_k$, the ODE solution x shall undergo a net increase (decrease) over the $(k+1)^{th}$ input cycle to follow. In other words, the $(k+1)^{th}$ map return point x_{k+1} shall be larger (smaller) than the kth map return point x_k. This is visualised by superimposing arrows, pointing to the east (west), on the $\Delta x_{k+1;k}$ *versus* x_k locus, within the upper (lower) half plane. Each crossing between the locus and the horizontal axis denotes an admissible fixed point $x^\star$ for the Poincaré map, which satisfies the equality $x^\star = \mathcal{P}(x^\star)$ therein. The net state change per cycle at a map fixed point is obviously null. A fixed point of a Poincaré map is asymptotically stable (unstable) if and only if the $\Delta x_{k+1;k}$ *versus* x_k locus crosses the horizontal axis with a negative (positive) slope. An asymptotically stable fixed point for the map identifies an asymptotically stable oscillatory solution for the original periodically forced continuous-time system. More specifically, it indicates the unchanged value, sampled from this asymptotic solution at the end of each input cycle. A good approximation for a $\Delta x_{k+1;k}$ *versus* x_k locus may be smartly obtained by running a large number of T-long numerical simulations of the forced ODE system, one for each initial condition x_0 in a set, which adequately covers the state existence domain $\mathcal{D}_x$, recording the state sample $x_1 \triangleq x(T)$ at the end of each test, plotting the net state change $\Delta x_{1;0} \triangleq x_1 - x_0$ *versus* the respective initial condition x_0 in each iteration, and finally applying some interpolation method to find the best fit for a curve joining the various points on the $\Delta x_{1;0}$ *versus* x_0 plane.

Here, the Poincaré map admits a triplet of fixed points, specifically $x_1^\star = 1.000919 \cdot 10^{24}$, $x_2^\star = 7.809066 \cdot 10^{24}$, and $x_3^\star = 7.389705 \cdot 10^{25}$. The left (right) outer stable one identifies the fixed value, which is obtained upon sampling the small (large)-amplitude oscillatory solution to the periodically forced ODE (1) at regular T-long time intervals, after transients vanish, as clarified shortly. Plot (c) shows [plots (e) and (g) show] the progressive approach of the solution x to the ODE (Eq. 1) toward the small (large)-amplitude oscillatory waveform, upon assigning the first value (the second and third values) from the set $\{6.5 \cdot 10^{24}, 9 \cdot 10^{24}, 3 \cdot 10^{29}\}$) to the initial condition x_0. As shown in plot (d), [respectively shown in plots (f) and (h)], the state solution in plot (c) [each of the state solutions in plots (e) and (g)] approaches an oscillation, whose maximum[4] is exactly the stable fixed point $x_1^\star$ ($x_3^\star$) of the Poincaré map [see plot (b)]. Although via extensive numerical explorations it is possible to infer how one may tailor the input parameter setting so as to induce bistability in a ReRAM cell, it would be better to develop a theoretical approach to serve this purpose. This is one of the key issues this manuscript aims to address[5]. In order to resolve this problem, the TA-SDR technique, a

1 Applying a positive (negative) voltage stimulus at the Pt electrode, while grounding the Ta electrode, a RESET (SET) resistance switching transition is induced in the Ta/TaO_x/Pt device stack manufactured in Jülich.

2 An ODE is said to be non-autonomous if it is forced by a non-constant input. Else, it is an autonomous system.

3 Importantly, the Poincaré map technique allows studying a periodically forced continuous-time system, which is equivalent to a second-order autonomous ODE, in which the time variable encodes one degree of freedom, through a simpler one-dimensional discrete-time system.

4 Note that, inverting the order of the RESET and SET pulses in the periodic voltage stimulus v_S, depicted in Figure 1A, the two stable fixed points for the new map, which would be extracted in this other excitation scenario, would correspond to the minima for two locally stable steady-state oscillations in the memory state.

5 Despite its high predictive accuracy, the SCPCM technique (Ascoli et al., 2023b) relies on numerical integrations, and, for this reason, is not employable to resolve this open question. It may be used, however, to verify the predictions from the time-averaging method, which holds validity only in periodic excitation scenarios, which induce small changes in the state per cycle Ascoli et al. (2022).

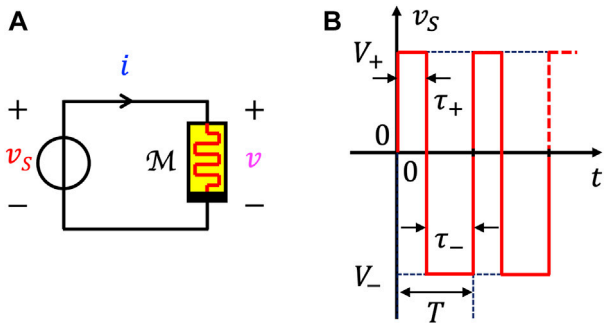

FIGURE 2
(A) Circuit setup for investigating the response of a voltage-controlled memristor $\mathcal{M}$ to the application of a periodic voltage stimulus v_S between its terminals. **(B)** Generic square pulse train-based voltage signal from the class of periodic stimuli, on which the local fading memory of the ReRAM cell from Jülich is explored via an in-depth theoretico-numerical analysis of the JART VCM model. Without loss of generality, a positive RESET (negative SET) voltage of amplitude V_+ (V_-) is applied across the memristor over the first (second) $\tau_+(\tau_-)$-long part of each cycle.

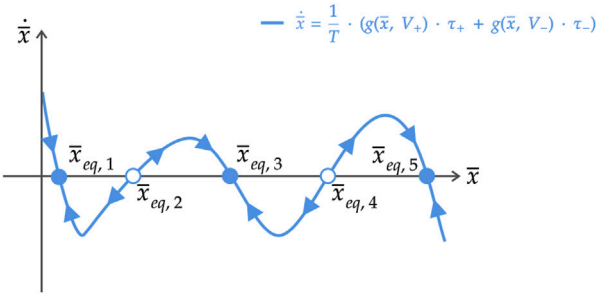

FIGURE 3
Exemplary illustration for the TA-SDR of a first-order memristor under periodic stimulation, as established in the test circuit of Figure 2A, from an AC voltage source v_S, generating a specific periodic square pulse train, of the kind shown in plot (b) of the same figure. Each filled (hollow) circle along the horizontal axis indicates an asymptotically stable (an unstable) equilibrium $\bar{x}_{eq}$ for the TA-SE (Eq. 7) associated with the particular ReRAM cell excitation case study.

powerful system-theoretic method, inspired to a recent bifurcation study (Pershin and Slipko, 2019) and referred to as the *time-averaging method* in the theory of non-linear dynamics (Guckenheimer and Holmes, 1983), shall be applied to the JART VCM model under the hypothesis that the respective input variable v is constrained to follow a periodic square pulse train stimulus v_S, composed of two square pulses of different polarity per cycle. A rigorous methodology is developed in this manuscript to determine how one may massage the shape of a periodic stimulus from this class in such a way to endow the nano-device with a variable number of stable oscillatory operating modes. Although bistability is the simplest form of local fading memory, the application of the proposed methodology reveals the possible coexistence of three steady-state oscillatory solutions for the ODE (Eq. 1) under suitable periodic perturbation. The capability of the ReRAM cell to exhibit a programmable multistable oscillatory response under suitable periodic stimulation may be harnessed for the hardware realisation of some innovative sensing and mem-computing concept in the future. The experimental demonstration of the capability of the ReRAM cell, set under the zooming lens in this paper, to act as one of two distinct oscillators, depending upon the initial condition, as reported in Section 7, is an encouraging step in the pursuit of this long-term goal.

3 The TA-SDR: a system-theoretic tool for the study of the response of first-order memristors to square pulse train stimuli

This section describes a powerful graphic method, which allows investigating the response of first-order nonlinear dynamical systems to AC periodic square pulse train-based excitations. It was introduced and applied to the Strachan model from Strachan et al. (2013) in an interesting numerico-analytical study (Pershin and Slipko, 2019) of the bifurcations, experienced by the TaO_x ReRAM cell, manufactured at Hewlett Packard Labs, under periodic stimuli of this kind, and later employed in a deep study (Messaris et al., 2023) of the high-frequency response of the same nano-device.

Without loss of generality, consider the DAE SET (Eqs 1, 2) of an extended first-order voltage-controlled memristor (Chua, 2018). The JART VCM model, revisited in Supplementary Appendix A.1, may be formulated in this form. An AC voltage source v_S is now inserted across the memristor $\mathcal{M}$, as depicted in Figure 2A. Let the source generate a periodic square pulse train, as sketched in Figure 2B, from $t = 0$ s. Over each period T, the stimulus consists of a pulse doublet, composed of a first-positive RESET pulse of height V_+ and width τ_+, and a second-negative SET pulse of height V_- and

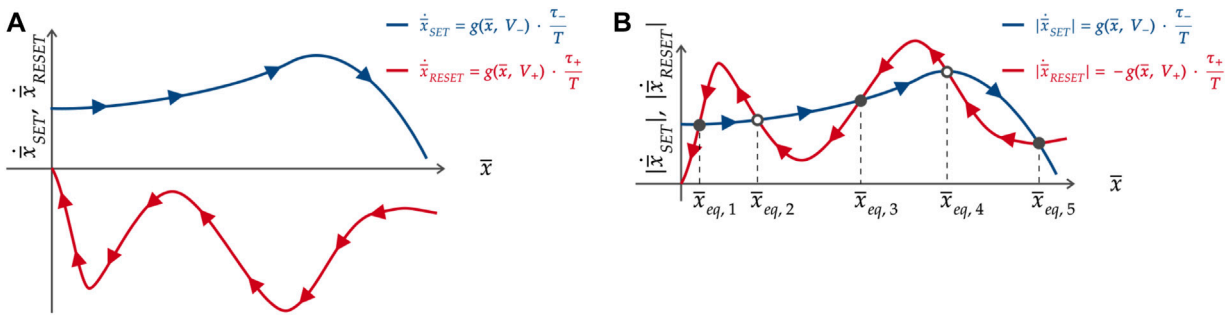

FIGURE 4
(A) Decomposition of the exemplary TA-SDR from Figure 3 into its two constitutive contributions, referred to as RESET and SET components, which are, respectively associated with the positive and negative square pulse, composing the time waveform of a given ReRAM cell stimulus, falling in the class from Figure 2B, over the first (second) τ_+ (τ_-)-long part of each cycle. The RESET (SET) component lies on the lower (upper) half of the $\dot{\bar{x}}$ *versus* $\bar{x}$ plane and is visualised by means of a red (blue) trace. As indicated by the arrows, pointing to the west (east) along the RESET (SET) locus, the time-average state $\bar{x}$ decreases (increases) under the effect of the positive (negative) rectangular pulse. **(B)** Plots of the moduli of the RESET and SET components, enabling the identification of the locations of all the admissible equilibria for the TA-SE (Eq. 7) through their intersections. The direction of the arrows along the RESET (SET) trace is kept unchanged relative to the direction of the arrows along the red (blue) locus in plot **(A)**. The asymptotic stability of an equilibrium for the TA-SE requires the SET (RESET) locus to be higher than the RESET (SET) locus to its left (right). A filled (hollow) circle is employed to mark each asymptotically stable (unstable) equilibrium for the TA-SE corresponding to the specific ReRAM cell excitation scenario under focus.

width τ_-. The time average $\bar{x}$ of the device memory state x over a period $T = \tau_+ + \tau_-$ of the voltage stimulus[6] changes over time according to

$$\bar{x}(t) = \frac{1}{T} \cdot \int_t^{t+T} x(\tau) d\tau. \tag{3}$$

Applying the Leibniz integral rule to Eq. 3, the time derivative of the time average state varies with time as

$$\dot{\bar{x}}(t) = \frac{x(t+T) - x(t)}{T}. \tag{4}$$

Now, integrating the state Eq. 1 over a period gives the following expression:

$$x(t+T) - x(t) = \int_t^{t+\tau_+} g(x(\tau), V_+) d\tau + \int_{t+\tau_+}^{t+\tau_+ + \tau_-} g(x(\tau), V_-) d\tau \tag{5}$$

$$\approx g(\bar{x}, V_+) \cdot \tau_+ + g(\bar{x}, V_-) \cdot \tau_-, \tag{6}$$

in which the last line assumes that within the time duration of a RESET (SET) pulse, the memory state undergoes[7] such a small decrease (increase) to justify its approximation via the respective time average, within the argument of the state evolution function in the first (second) time integral, without introducing a noticeable loss in computation accuracy. Finally, substituting Eq. 6 into Eq. 4 allows deriving the TA-SE, specifically

$$\dot{\bar{x}} = \frac{1}{T} \cdot g(\bar{x}, V_+) \cdot \tau_+ + \frac{1}{T} \cdot g(\bar{x}, V_-) \cdot \tau_-, \tag{7}$$

which[8] governs the time evolution of the time average state $\bar{x}$ upon forcing the input v to the ODE (Eq. 1) to follow a specific square pulse train voltage stimulus v_S from the class illustrated in Figure 2B. Assuming that the choice for the pulse doublet parameters, namely, the quartet $\{V_+, \tau_+, V_-, \tau_-\}$, ensures a good accuracy for the approximation in Eq. 6, the determination of the equilibria of the TA-SE (7), together with the study of their stability properties, allows identifying all the possible levels, around which the memory state of the periodically driven ReRAM cell may be ever found to oscillate asymptotically. The initial condition x_0, assigned to the memory state x, related to the conductance G (x_0, 0), programmed into the device preliminarily, would determine which of the admissible locally stable oscillatory solutions for the memory state itself would be observed during the periodic test after transients decay to zero.

An equilibrium $\bar{x}_{eq}$ for the TA-SE (Eq. 7) satisfies the constraint $\dot{\bar{x}}|_{\bar{x}=\bar{x}_{eq}} = 0$ and corresponds to an admissible oscillation for the steady-state solution of the state Eq. 1. The equilibrium is asymptotically stable (is unstable) if and only if $(d\dot{\bar{x}}/d\bar{x})|_{\bar{x}=\bar{x}_{eq}}$ is negative (positive). Plotting the time-average state evolution function, composing the right hand side of the TA-SE, *versus* the time average state provides the locus of $\dot{\bar{x}}$ *versus* $\bar{x}$, which is referred to as TA-SDR. This graph enables gaining precious insights into the dynamics of the time-average state without solving the TA-SE itself. Importantly, as it goes for the TA-SE (7), TA-SDR is strictly associated with a particular periodic square pulse train-based voltage signal v_S, falling in the class defined in Figure 2B, and acting as the input v to the state Eq. 1 of the device model. Arrows, pointing to the east (west), are superimposed

6 For the sake of simplicity, $\bar{x}$ shall be referred to as the *time-average state* in the remainder of the paper.

7 As anticipated in Section 2, when a positive (negative) voltage v is let to fall between the Ta and Pt electrodes of the device stack from Jülich, the device undergoes a RESET (SET) transition. Moreover, as the state evolution function $g(x, v)$ in the JART model is *anti-sign invariant* (Chua, 2018), implying $g(x, v) < (>)0$ for $v > (<)0$, the state variable decreases (increases) in a RESET (SET) transition. In fact, in such a model, $x = x_{min}$ ($x = x_{max}$) corresponds to the fully-RESET (fully-SET) state for the device.

8 The right hand side of Eq. 7 may be referred to as the *time-average state evolution function*.

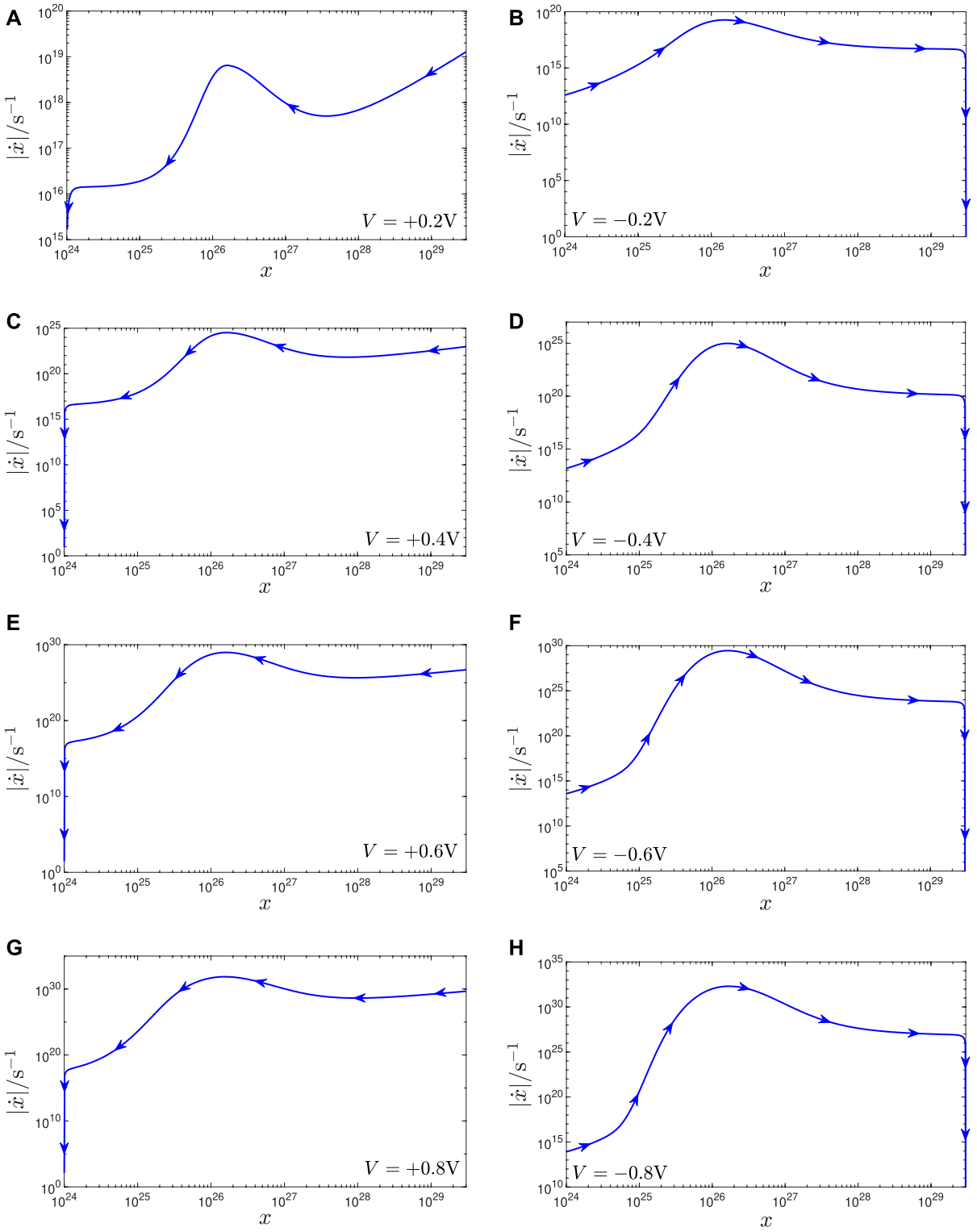

FIGURE 5
(A, C, E, G) ((B, D, F, H)) Family of $|g(x, V)|$ *versus* x loci, for $V = V_{+}(V_{-}) \in \{+(-)0.2, +(-)0.4, +(-)0.6, +(-)0.8\}$V, according to the predictions of the JART VCM model. The first (latter) family illustrates the multi-decade variation range for the RESET (SET) switching speed across the state existence domain for a number of positive (negative) DC inputs. Together, the RESET and SET SDRs, shown in the plots along the top and bottom rows, respectively, compose the DRM of the ReRAM cell.

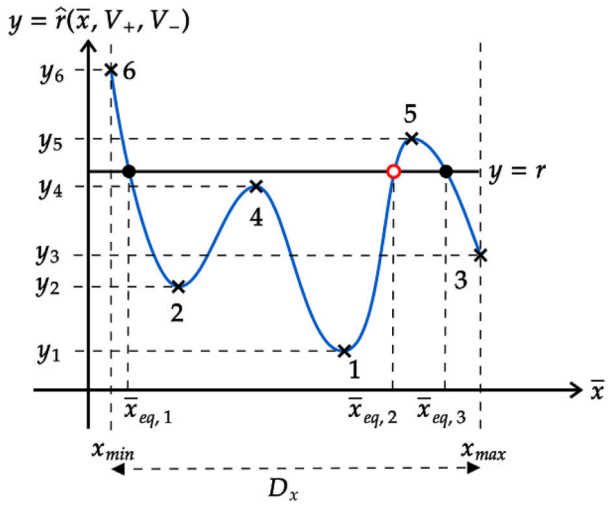

FIGURE 6
Representative diagram, illustrating the basics of the methodology, which is adopted in this work to study *the bifurcations in the number of equilibria for the TA-SE under pulse width ratio sweep*, given a preliminary selection for the remaining stimulus parameters, i.e., V_+ and V_-. Blue curve: locus of the function $y = \hat{r}(\bar{x}, V_+, V_-)$ *versus* the time-average state $\bar{x}$. Horizontal black line: graph of the function $y = r$ for a generic choice of the pulse width ratio. With reference to the blue cross markers, the ordinates of the local minima and maxima for $y = \hat{r}(\bar{x}, V_+, V_-)$, together with the values, which this function assumes at the lower and upper bounds of the memory state existence domain, are sorted in ascending order from the lowest, i.e., y_1, to the highest, i.e., y_6. It can be easily demonstrated that a time-average state value $\bar{x}_{eq}$, at which the equality, expressed by Eq. 12, applies, corresponds to an asymptotically stable (an unstable) equilibrium for the TA-SE, as indicated through a black-filled (red-hollow) circle in this diagram, if and only if the slope of the function $y = \hat{r}(\bar{x}, V_+, V_-)$ is negative (positive) therein. To name but one example, the line $y = r$, corresponding to a choice for the pulse width ratio between y_4 and y_5, crosses the graph of $y = \hat{r}(\bar{x}, V_+, V_-)$ in three locations, where $\bar{x}$ assumes values from the set $\{\bar{x}_{eq,1}, \bar{x}_{eq,2}, \bar{x}_{eq,3}\}$, revealing the existence of a triplet of TA-SE equilibria, of which each of the outer ones (the inner one) is asymptotically stable (unstable).

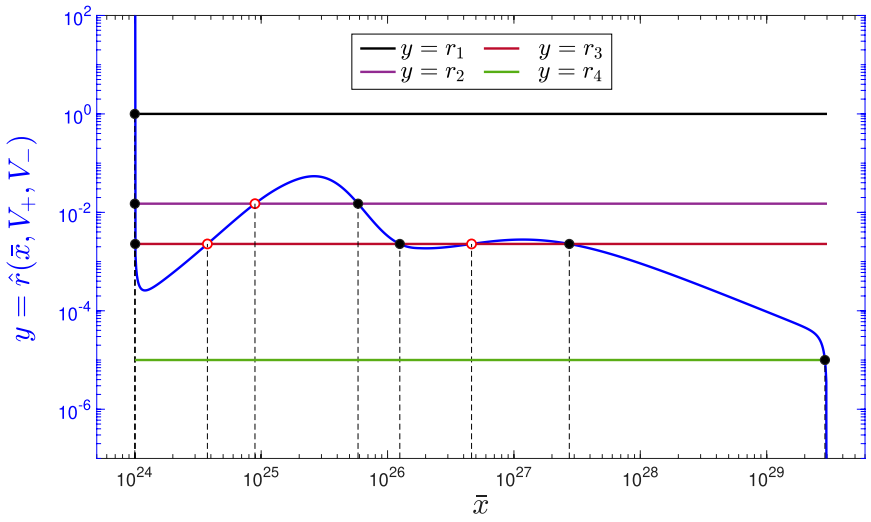

FIGURE 7
Blue trace: locus of $\hat{r}(\bar{x}, V_+, V_-)$ *versus* $\bar{x}$ over the memory state existence domain $\mathcal{D}_x \in [x_{min}, x_{max}]$, with $x_{min} = 1 \cdot 10^{24}$ and $x_{max} = 3 \cdot 10^{29}$, for $(V_+, V_-) = (+0.31\ V, -0.2\ V)$. It crosses the black horizontal line $y = r_1 = 1$ in one point, whose abscissa constitutes the only equilibrium, which the TA-SE admits under the input parameter triplet (V_+, V_-, r_1). Three are the crossings between the blue curve and the violet horizontal line $y = r_2 = 1.5 \cdot 10^{-2}$. The abscissas of these crossings provide a set of three admissible equilibria for the TA-SE under the input parameter triplet (V_+, V_-, r_2). The brown horizontal line $y = r_3 = 2.3 \cdot 10^{-3}$ meets the $\hat{r}(\bar{x}, V_+, V_-)$ *versus* $\bar{x}$ locus in five points, whose abscissas identify five possible equilibria for the TA-SE under the input parameter triplet (V_+, V_-, r_3). Finally, there exists one and only one point of intersection between the blue trace and the green horizontal line $y = r_4 = 1 \cdot 10^{-5}$. Its abscissa represents the only equilibrium for the TA-SE associated with the input parameter triplet (V_+, V_-, r_4). For each of the four case studies, a black (red) circle is employed to mark the position of a stable (an unstable) equilibrium for the respective TA-SE.

on a locus of this kind, where it visits the upper (lower) half of the $\dot{\bar{x}}$ *versus* $\bar{x}$ plane so as to indicate an increase (a decrease) in the time-average state when the right hand side of Eq. 7 is positive (negative). Each intersection of TA-SDR with the horizontal axis identifies a possible equilibrium $\bar{x}_{eq}$ for the respective TA-SE. The equilibrium is asymptotically stable (is unstable) if and only if the TA-SDR has a negative (positive) slope as it goes through it. Figure 3 shows the TA-SDR of a first-order memristor, which, driven periodically by a square pulse train-based voltage stimulus of the form depicted in Figure 2B, as established by the test circuit set-up protocol, illustrated in plot (a) of the same figure, is expected to operate according to one of three possible oscillatory modes, after transients decay to zero, depending upon the initial condition x_0. In fact, the exemplary TA-SDR predicts the existence of five equilibria for the respective TA-SE, specifically $\bar{x}_{eq,1}, \bar{x}_{eq,2}, \ldots, \bar{x}_{eq,5}$, of which those identified by odd (even) numbers are asymptotically stable (are unstable). In case the stimulus parameters are chosen in such a way that approximating the state with its time average within each integrand in Eq. 5 does not jeopardise the computational accuracy of the respective time integral, the memory state of the periodically driven ReRAM cell shall oscillate around one of three possible levels, specifically $\bar{x}_{eq,1}$, $\bar{x}_{eq,3}$, or $\bar{x}_{eq,5}$, after transients vanish, depending upon the initial condition x_0. In particular, if x_0 is chosen in such a way that $\bar{x}_0 \triangleq \bar{x}(0)$, i.e., as follows from Eq. 3, the initial value for the time average of the solution to the ODE (Eq. 1), as computed across the first input cycle, is lower (higher) than $\bar{x}_{eq,2}$ ($\bar{x}_{eq,4}$), then x shall asymptotically oscillate around $\bar{x}_{eq,1}$ ($\bar{x}_{eq,5}$). If, on the other hand, x_0 is set so that $\bar{x}_0$ is found to lie within the range $(\bar{x}_{eq,2}, \bar{x}_{eq,4})$, then the mean value of the steady-state oscillation in x shall be $\bar{x}_{eq,3}$.

In the next section, a rigorous methodology, based upon the system-theoretic TA-SDR analysis tool, shall be set in place to massage the four parameters of the AC periodic pulse train stimulus of Figure 2B in such a way to induce the coexistence of a variable number of distinct steady-state oscillatory solutions for the memory state of the ReRAM cell under the zooming lens in this manuscript.

4 A systematic technique to endow the periodically driven memory cell with a variable number of oscillatory operating modes

Let us commence this section by introducing an alternative way to determine the equilibria of TA-SE and study their local stability properties.

4.1 TA-SDR decomposition

The TA-SE (Eq. 7) can be recast as the sum between a *RESET component* and a *SET component* via

$$\dot{\bar{x}} = \dot{\bar{x}}_{\mathrm{RESET}} + \dot{\bar{x}}_{\mathrm{SET}}. \tag{8}$$

The first and latter contributions are, respectively, defined as

$$\dot{\bar{x}}_{\mathrm{RESET}} = \frac{1}{T} \cdot g(\bar{x}, V_+) \cdot \tau_+, \text{ and} \tag{9}$$

$$\dot{\bar{x}}_{\mathrm{SET}} = \frac{1}{T} \cdot g(\bar{x}, V_-) \cdot \tau_-. \tag{10}$$

The RESET (SET) component is, in fact, a scaled version of the right hand side of the SE[9] (Eq. 1), with the time-average state in place for the state, under a positive (negative) DC voltage $V = V_+$ (V_-). As an exemplary case study, the RESET and SET components, whose sum results in TA-SDR, illustrated in Figure 3, are, respectively, shown through a solid red and blue trace as a function of the time-average state in Figure 4A. Arrows along the first (latter) component point toward the west (the east), revealing that the physics laws, governing the OFF (ON) dynamics, establish a decrease (an increase) for the time-average state over the time interval τ_+ (τ_-), when the positive (negative) square pulse of height V_+ (V_-) perturbs the memristor. Far more insightful is the illustration of Figure 4B, showing the moduli of the RESET and SET components from plot (a) of the same figure. Note that in this new graphic representation, the direction of motion for the time-average state along the RESET (SET) trace still takes into account the negative (positive) polarity of the contribution expressed by Eqs 9, 10. Naturally, the TA-SE, cast as reported in Eq. 8, admits an equilibrium $\bar{x}_{eq}$ at the abscissa of any intersection between the moduli of the RESET and SET components, i.e., at each time-average state, where[10] $\dot{\bar{x}}_{\mathrm{SET}}|_{\bar{x}_{eq}} = -\dot{\bar{x}}_{\mathrm{RESET}}|_{\bar{x}_{eq}}$, which, employing Eqs 9, 10, can be expressed as

$$g(\bar{x}, V_-) \cdot \tau_- = -g(\bar{x}, V_+) \cdot \tau_+. \tag{11}$$

Moreover, the equilibrium is asymptotically stable if and only if the ON (OFF) dynamics are dominant over the OFF (ON) dynamics to its left (right). The decomposition of the TA-SE into its SET and RESET components is at the basis of a systematic methodology to craft the periodic pulse train stimulus, to be applied across the nano-device, so as to endow its memory state with oscillatory monostable or multistable response, as elucidated in Section 4.3. Before presenting the methodology, it is worth exploring the state evolution function $g(x, v)$ *versus* state x loci under sweep in the positive (negative) DC value V_+ (V_-), assigned to the input variable to the ODE (Eq. 1). In fact, the larger the difference

9 Referring, without loss of generality, to an anti-sign invariant state evolution function, the locus of the right hand side of the SE (Eq. 1) *versus* the memory state for a given positive (negative) DC voltage $v = V = V_+(V_-)$ is referred to as a RESET (SET) state dynamic route, RESET SDR (SET SDR) for short. The families of RESET and SET SDRs compose the DRM of the first-order memristor.

10 Numerical investigations, based upon the JART VCM model, already revealed (Ascoli et al., 2022) that the level, around which the memory state x of the TaO_x ReRAM cell, manufactured at FZJ, is found to oscillate, after transients vanish, for a given initial condition x_0, under the effect of a purely-AC periodic triangular voltage stimulus v_S of suitable amplitude $\hat{v}_S$ and frequency f_S (Messaris et al., 2023), is approximately equal to the abscissa of a specific intersection between the moduli of the RESET and SET SDRs, respectively, extracted from the memristor DRM upon setting the DC voltage V to a positive V_+ and negative V_- value of common modulus $\hat{v}_S$.

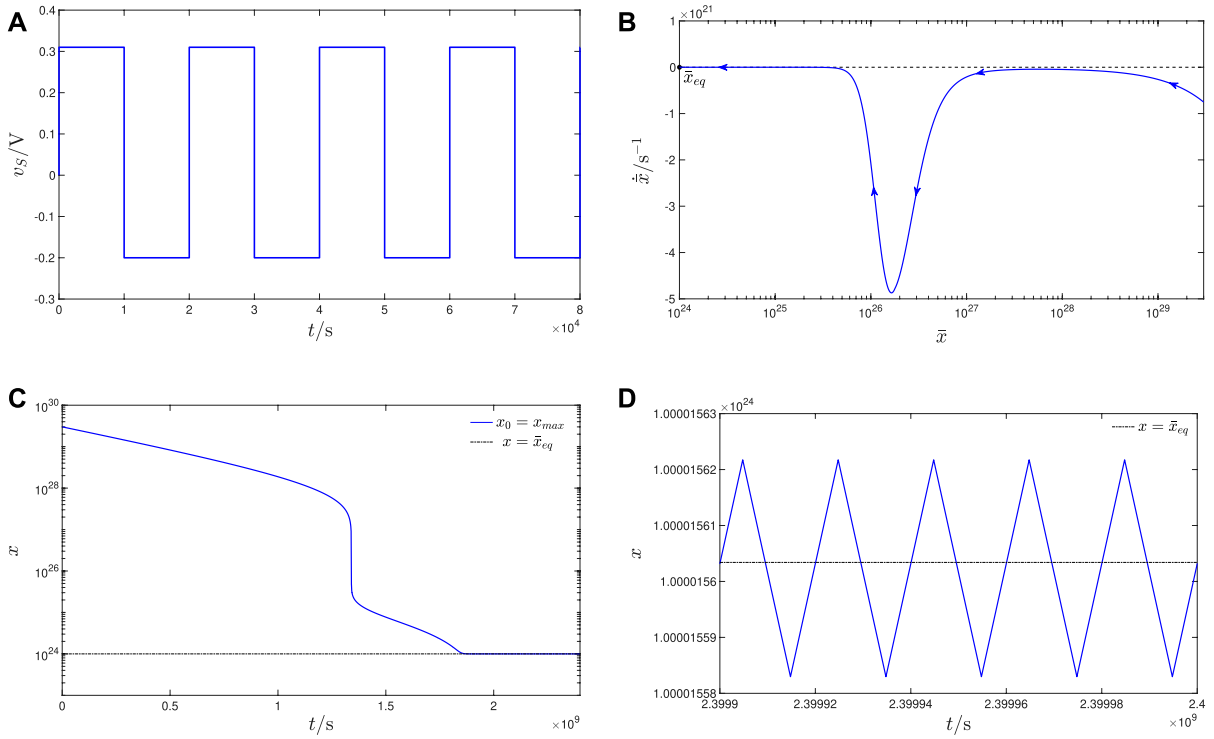

FIGURE 8
(A) Time waveform of the periodic voltage signal v_S, which, let fall across the ReRAM cell, enforces its steady-state operation as a monostable oscillator around the fully-RESET state (case study 1.1). The first (second) positive (negative) RESET (SET) pulse in each cycle of the train features an amplitude V_+ (V_-) of +0.31 V (−0.2 V), as established via Figure 7, for all case studies in this section. The common value of $10 \cdot 10^3$ s is assigned to the RESET τ_+ and SET τ_- pulse widths, implying $T = \tau_+ + \tau_- = 20 \cdot 10^3$s and $r = r_1 = 1$. **(B)** TA-SDR, associated with the input from **(A)** and predicting a single GAS equilibrium $\bar{x}_{eq}$ for the TA-SE at a location, identified by the black filled circle marker, standing at $1.000015603 \cdot 10^{+24}$, which is close to yet above the lowest admissible memory state value $x_{\min} = 1 \cdot 10^{+24}$. This is in accordance with the insights, gained earlier from Figure 7, where, the black horizontal line $y = r_1 = 1$ crosses the $\hat{r}(\hat{x}, V_+, V_-)$ *versus* $\hat{x}$ locus, associated with the input pulse height pair (V_+, V_-) = (+0.31 V, −0.2 V), in one point, with an abscissa equal to the TA-SE equilibrium $\bar{x}_{eq}$, only. **(C)** (**(D)**) Transients (steady-state) in the time course of the solution to the JART VCM ODE (Eq. 1) (Bengel et al., 2022) under $v = v_S$, with v_S as in plot **(A)**, and for $x_0 = x_{\max}$. As expected, while exhibiting a monostable steady-state oscillatory behaviour, the memristor operates around the fully-RESET state.

between the shapes of the SET SDRs and the shapes of the RESET SDRS and the higher the tunability of the loci within each of these two families, the simpler would be to modulate the two components of the TA-SE so as to enforce a desired number of intersections between the graphs of their moduli along the state existence domain.

4.2 Impact of the positive/negative DC voltage on the shape of the ReRAM cell RESET/SET SDR

The TA-SE (Eq. 7), corresponding to a given square pulse train excitation, is a linear combination of two copies of the state evolution function. The first (latter) copy is expressed in terms of the time-average state and of the positive (negative) DC voltage, representing the height of the first RESET (second SET) pulse in the waveform of the AC periodic input over each cycle, and is weighted by the ratio between the width of the same pulse and the period of the stimulus. Moreover, the intersections between the loci of the moduli of these two terms identify the admissible equilibria for the TA-SE. In order to develop a strategy to endow the TA-SE with a desired number of stable equilibria, falling within the memory state existence domain, it is of interest to explore the influence of the positive (negative) value $V_+(V_-)$, assigned to a DC voltage V, employed within the argument of the state evolution function, on the shape of the RESET (SET) SDR. Plots (a), (c), (e), and (g) ((b), (d), (f), and (h)) of Figure 5, respectively, show the RESET (SET) SDR associated with the first, second, third, and fourth V_+ (V_-) values from the set {+(−)0.2, + (−)0.4, + (−)0.6, + (−)0.8}V. A couple of important points stand out from the graphical inspection of these plots. First, differently from what is the case for other ReRAM cells (Ascoli et al., 2023a), the shapes of the loci, associated with positive-valued DC stimuli, do not differ so significantly from those, associated with negative-valued DC stimuli, complicating the identification of a simple strategy to vary the number of crossings between the moduli of the loci of the SET and RESET TA-SE components. Second, as established by the boundary conditions, included in the JART VCM model, which is reviewed in Supplementary Appendix A.1, while the memory state approaches the lower (upper) bound in its existence domain during a RESET (SET) transition, its deceleration is rather abrupt, as demonstrated by the sudden fall of either locus on the left (right) column of plots in Figure 5 in the neighbourhood of the minimum (maximum) allowable state value. On the other hand, the memory state does not accelerate

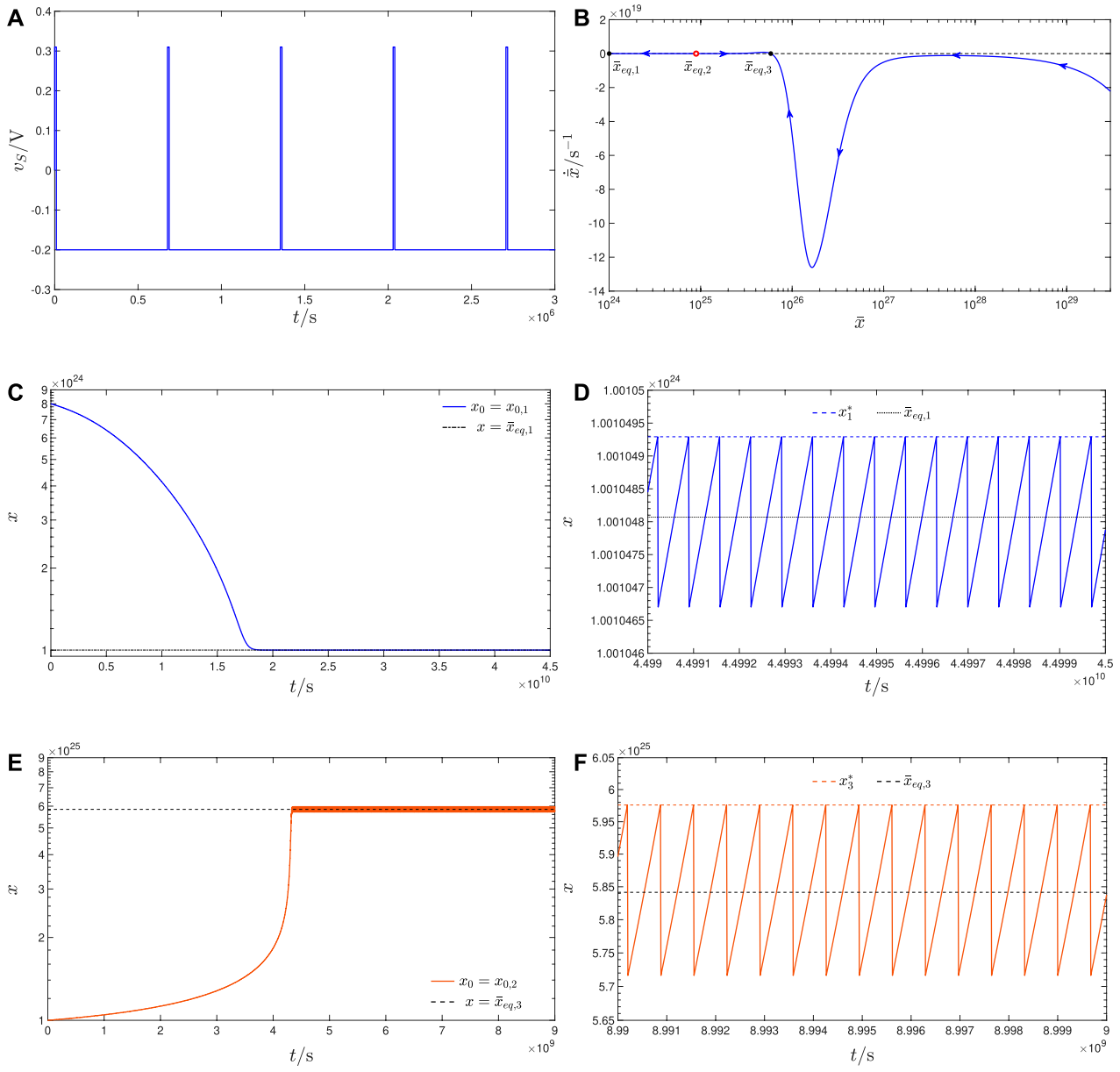

FIGURE 9
(Continued).

(decelerate) in a similarly dramatic way as it increases (decreases) from values close to the lower (upper) bound in its existence domain over the course of a SET (RESET) process, as revealed by the relatively mild ascent (descent) of either locus on the right (left) column of plots in Figure 5 in the neighbourhood of the minimum (maximum) allowable state value. The rather different behaviour of the SET and RESET SDRs around the lower (upper) bound in the state existence domain explains why it is relatively simple to choose the stimulus parameters, namely, V_+, τ_+, V_-, and τ_-, in such a way to enforce one intersection between the loci of the moduli of the SET and RESET TA-SE components in the vicinity of the smallest (highest) admissible state value. Massaging conveniently the four input parameters, it is further possible to ensure that the modulus of the RESET (SET) term in the linear combination on the right hand side of the TA-SE is larger than the modulus of the other SET (RESET) term to the right (left) of the lower (upper) bound in the state existence domain, which ensures that the solution to the ODE (Eq. 1) would exhibit a steady-state oscillatory waveform around the fully-RESET (fully-SET) state, as revealed, for example, in the monostability case study 1.1 (1.4) from Section 5.1.1 (5.1.4). However, it is fair to admit that, in an excitation scenario from the first (latter) kind, the ReRAM cell typically exhibits slower and slower dynamics as the respective memory state gets closer and closer to its minimum (maximum) allowable value. Therefore, the practical exploitation of a device oscillatory mode, implying the excursion of the memory state around a level in the proximity of the lower (upper) bound in its existence domain, is questionable. Moreover, in general, it is advisable to operate the device away from its fully-RESET (fully-SET) state.

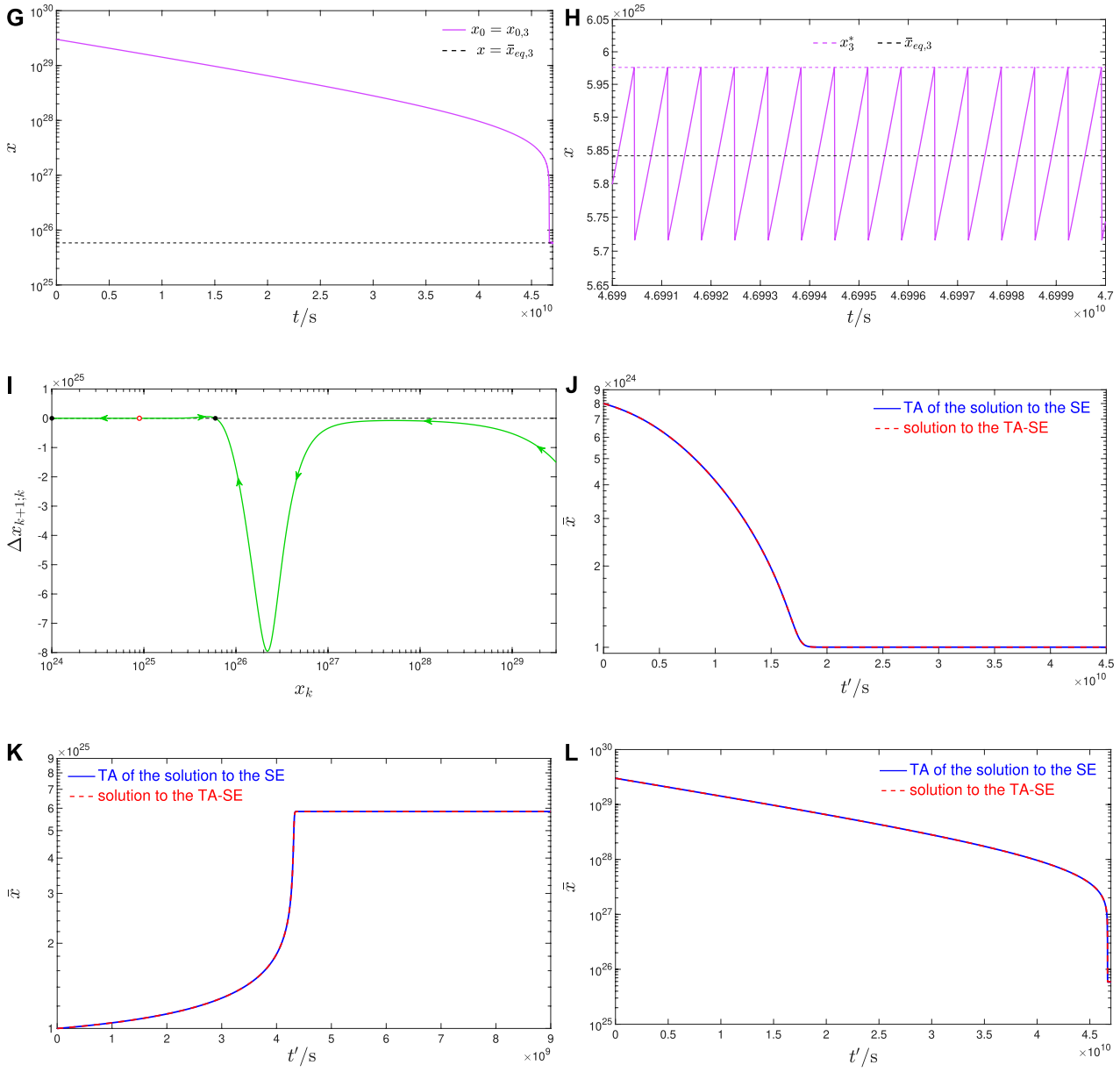

FIGURE 9
(Continued). **(A)** Time course of the two-pulse-per-cycle train voltage signal, which induces a bistable oscillatory response in the ReRAM cell (case study 1.2). The RESET τ_+ and SET τ_- pulse width parameters, identifying unequivocally the AC periodic stimulus, together with the fixed values + 0.31 V and −0.2 V, set in turn for the RESET V_+ and SET V_- pulse amplitudes, in the scenario Figure 7 refers to, are taken here as $1 \cdot 10^4$s, and $6.667 \cdot 10^5$s, respectively. **(B)** Resulting TA-SDR for the periodically driven ReRAM cell, revealing the existence of three equilibria, specifically $\bar{x}_{eq,1} = 1.00105 \cdot 10^{24}$, $\bar{x}_{eq,2} = 8.93240 \cdot 10^{24}$, and $\bar{x}_{eq,3} = 5.84158 \cdot 10^{25}$, for the respective TA-SE. A filled (hollow) black circle is used to mark each of the outer locally stable equilibria (the inner unstable equilibrium). **(C, E, G)** Transients in the time evolution of the memory state, as resulting from the numerical integration of the JART VCM model (consult Supplementary Appendix A.1 for details) under the stimulation protocol, envisaged in the case study under examination, upon pre-setting x_0 to the first, second, and third initial conditions from the set $S_1 = \{x_{0,1}, x_{0,2}, x_{0,3}\} = \{8 \cdot 10^{24}, 1 \cdot 10^{25}, 3 \cdot 10^{29}\}$. **(D, F, H)** Oscillatory steady states for the time waveforms from plots **(C, E, G)**, respectively. The mean value of the oscillation in the memory state from plot **(D)** (from either of plots **(F, H)**) agrees with the outer left (right) crossing $\bar{x}_{eq,1}$ ($\bar{x}_{eq,3}$) of the TA-SDR from plot **(B)** with the horizontal axis. **(I)** SCPCM of the JART VCM ODE under $v = v_S$, as shown in plot **(A)**. The fixed points of the Poincaré map, from which the $\Delta x_{k+1;k}$ *versus* $x(k)$ locus was extracted, are $x_1^* = 1.00105 \cdot 10^{24}$, $x_2^* = 8.93292 \cdot 10^{24}$, and $x_3^* = 5.97593 \cdot 10^{25}$. Although the second point in this triplet is unstable, the first (third) one is asymptotically stable, identifying the maximum of the steady-state oscillation in plot **(D)** (in either of plots **(F)** and **(H)**) as it descends from the order of the two square pulses, composing the train stimulus in each period, and exciting first the RESET and then the SET device kinetics over the cycle. **(J, K, L)** Proof of evidence for the accuracy of the approximation, which, converting Eq. 5 into Eq. 6, enabled to reduce Eq. 4 into the TA-SE (Eq. 7), for case study 1.2. The first, second, and third plots from this triplet, respectively, demonstrate how the time average of the solution x to the SE (Eq. 1), adapted to the JART VCM model, and initiated from the first, second, and third initial conditions x_0 from the set S_1, evolves in time from the beginning of the second cycle in a practically equivalent fashion as the solution $\bar{x}$ to the TA-SE (Eq. 7), adapted to the same model, and initiated in turn from the first, second, and third initial condition $\bar{x}_0$ belonging to the set $\{8 \cdot 10^{24}, 1 \cdot 10^{25}, 3 \cdot 10^{29}\}$, and corresponding to the time average of the trace in plots **(C, E, G)** over the first input cycle according to Eq. 3. For each of the three cases, the datasets, corresponding to the first and latter solutions, are visualised in solid blue and red dashed line styles, respectively, against a new time variable defined as $t' \triangleq t - T$.

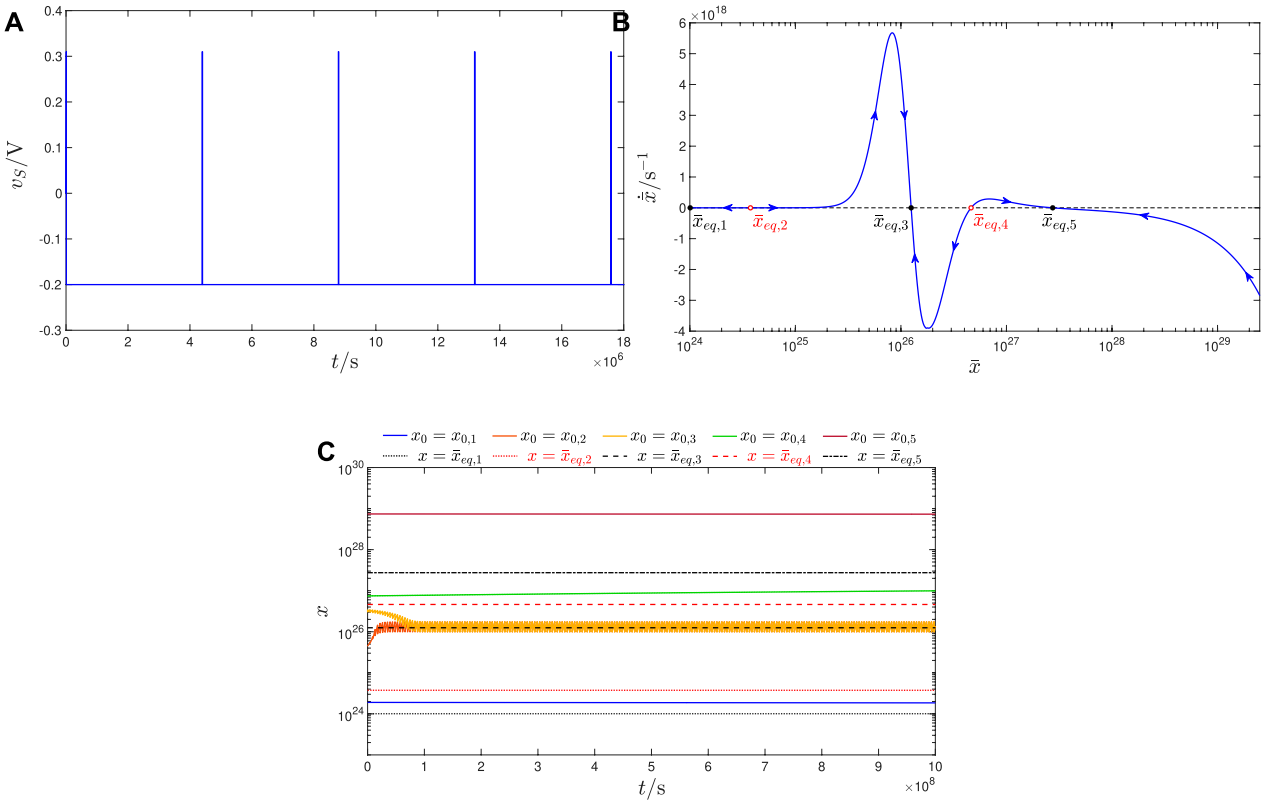

FIGURE 10
(A) Two-pulse-per-cycle periodic voltage signal v_S, to be applied across the TaO_x nanodevice so as to endow it with a tristable oscillatory behaviour (case study 1.3). The pulse height–width pair for the first (second) positive (negative) RESET (SET) pulse in each period of the stimulus is $(V_+, \tau_+) = (+0.31\ \mathrm{V}, 10 \cdot 10^3\mathrm{s})$ $((V_-, \tau_-) = (-0.2\ \mathrm{V}, 4.385 \cdot 10^6\mathrm{s}))$. Here, $r = r_3 = 2.3 \cdot 10^{-3}$, while $T = \tau_+ + \tau_- = 4.395 \cdot 10^6\mathrm{s}$. **(B)** TA-SDR of the ReRAM cell under the periodic excitation illustrated in **(A)**. Five are the intersections between the TA-SDR and the horizontal axis, specifically $\bar{x}_{eq,1} = 1.007 \cdot 10^{+24}$, $\bar{x}_{eq,2} = 3.756 \cdot 10^{+24}$, $\bar{x}_{eq,3} = 1.250 \cdot 10^{+26}$, $\bar{x}_{eq,4} = 4.621 \cdot 10^{+26}$, and $\bar{x}_{eq,5} = 2.743 \cdot 10^{+27}$, which correspond to the crossings between the brown horizontal line $y = r_3$ and the blue-coloured $\hat{r}(\bar{x}, V_+, V_-)$ *versus* $\bar{x}$ locus for $(V_+, V_-) = (+0.31\ \mathrm{V}, -0.2\ \mathrm{V})$, as shown in Figure 7. The equilibria, identified by odd (even) numbers, are asymptotically stable (are unstable), as indicated via black filled (red hollow) circles. **(C)** Transitory dynamics of the solution to the JART VCM ODE (Bengel et al., 2022) for each initial condition x_0 from the set $S_2 \triangleq \{x_{0,1}, x_{0,2}, x_{0,3}, x_{0,4}, x_{0,5}\} = \{1.9 \cdot 10^{24}, 4.6 \cdot 10^{25}, 3.5 \cdot 10^{26}, 7.5 \cdot 10^{26}, 7.4 \cdot 10^{28}\}$, under the application of the above-specified voltage stimulus across the ReRAM cell from $t = t_0 = 0\mathrm{s}$ to $t = 1 \cdot 10^9\mathrm{s}$, which covers just over 227 input cycles. Although the solutions, initiated from $x_{0,2}$ and $x_{0,3}$, attain the steady state, in particular the same, before the end of the simulation, this is not the case for the other three traces. As shown in Figure 11, the time spans, necessary for these five signals to converge to the respective asymptotic oscillations, may differ by orders of magnitude, which highlights the complex slow/fast dynamical behaviour of the ReRAM cell manufactured at FZJ. The horizontal dotted, dashed, and dash-dotted black (dotted and dashed red) lines, respectively, indicate the locations of the outer left $\bar{x}_{eq,1}$, inner $\bar{x}_{eq,3}$, and outer right $\bar{x}_{eq,5}$ locally stable (left $\bar{x}_{eq,2}$ and right $\bar{x}_{eq,4}$ unstable) TA-SE equilibria within the memory state existence domain $\mathcal{D}_x$. The unstable TA-SDR equilibria are closely related to the initial conditions, which, together with $x_{\min}$ and $x_{\max}$, separate the basins of attraction of the three admissible locally stable steady-state oscillatory solutions, shown in Figures 11B, D, F (refer to the concept, expressed at the end of Section 3, for details).

Far more interesting, yet harder, is to craft the square pulse train stimulus in such a way to induce the asymptotic emergence of at least one oscillatory state solution unaffected by the boundary conditions, and thus undergoing a periodic excursion across a real-valued range, falling well within its admissible existence domain, as shown, for example, in the multistability case study 1.2 (1.3) from Section 5.1.2 (5.1.3), where, taking into account that stable and unstable equilibria of a TA-SE alternate one after the other, as shown in the representative illustration of Figure 3, the moduli of the loci of the SET and RESET TA-SE components are enforced to feature as many as three (five) crossings, in order for the solution to the state Eq. 1 to exhibit a bistable (tristable) oscillatory behaviour after transients decay to zero. The next section presents a rigorous strategy to shape the AC periodic square pulse train input, applied to the JART VCM model, in such a way to endow its state variable with a monomodal or multimodal oscillatory response.

4.3 A rigorous approach to induce monostability or multistability in the memristor oscillatory response to square pulse train stimulation

Equation 11, expressing the condition for a crossing between the loci of the moduli of the SET and RESET TA-SE components to appear at a given time-average state value, say at $\bar{x} = \bar{x}_{eq}$, may be rearranged in the form

$$r = \hat{r}\left(\bar{x}_{eq}, V_+, V_-\right), \tag{12}$$

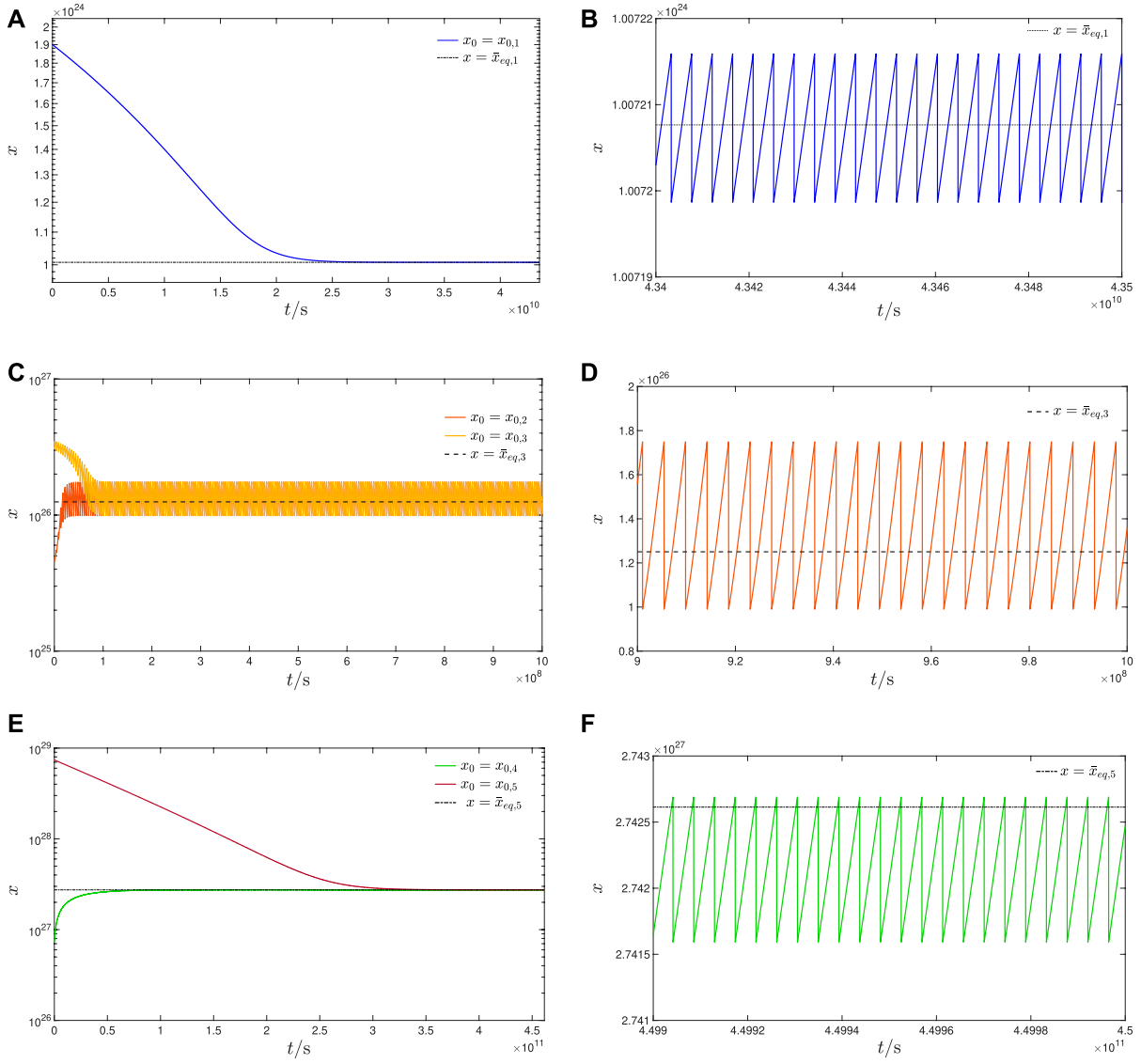

FIGURE 11
(A, C, E) Time waveform of the memory state x of the ReRAM cell, modelled by means of the JART VCM mathematical description (Bengel et al., 2022), as, respectively, recorded during transient simulations of the test circuit of Figure 2A over 250, 10,000, and 105,000 cycles of the AC periodic voltage stimulus, illustrated in Figure 10A, as envisaged in case study 1.3, when the first, second or third, and fourth or fifth value from the set $S_2 \triangleq \{x_{0,1}, x_{0,2}, x_{0,3}, x_{0,4}, x_{0,5}\} = \{1.9 \cdot 10^{24}, 4.6 \cdot 10^{25}, 3.5 \cdot 10^{26}, 7.5 \cdot 10^{26}, 7.4 \cdot 10^{28}\}$ is, in turn, assigned to the device initial condition x_0. In the first, second, and third plots from this triplet, the horizontal dotted, dashed, and dash-dotted black line marks, respectively, the location of the outer left $\bar{x}_{eq,1}$, of the inner $\bar{x}_{eq,3}$, and of the outer right $\bar{x}_{eq,5}$ locally stable TA-SE equilibria. **(B, D, F)** Steady states of the JART VCM ODE solutions from plots **(A, C, E)**, respectively. Importantly, as may be evidenced from plots **(D, F)**, boundary conditions have no impact on the steady-state dynamics of the periodically forced ReRAM cell in two of its three possible oscillatory operating modes.

where

$$r \triangleq \frac{\tau_+}{\tau_-} \tag{13}$$

stands for the ratio between the width of the positive RESET pulse and the width of the negative SET pulse, while

$$\hat{r}(\bar{x}, V_+, V_-) \triangleq -\frac{g(\bar{x}, V_-)}{g(\bar{x}, V_+)} \tag{14}$$

denotes the modulus of the ratio between two copies of the state evolution function, evaluated at a common time-average state $\bar{x}$ but at different DC voltages. Specifically, the copy at the numerator (denominator) is computed at the negative (positive) bias voltage, corresponding to the height of the SET (RESET) input pulse. The new formula (Eq. 12) for the existence condition of a TA-SE equilibrium reduces by one, the cardinality of the input parameter set to be explored in the determination of the number of possible crossings between the loci of the moduli of the SET and RESET TA-SE components. In fact, under the hypothesis that the height and width of each of the two square pulses, composing the periodic voltage stimulus over each cycle, are sufficiently small to ensure the accuracy of the approximation in Eq. 6, the number of admissible asymptotic oscillatory solutions for the memory state of the periodically driven ReRAM cell depends now solely upon the

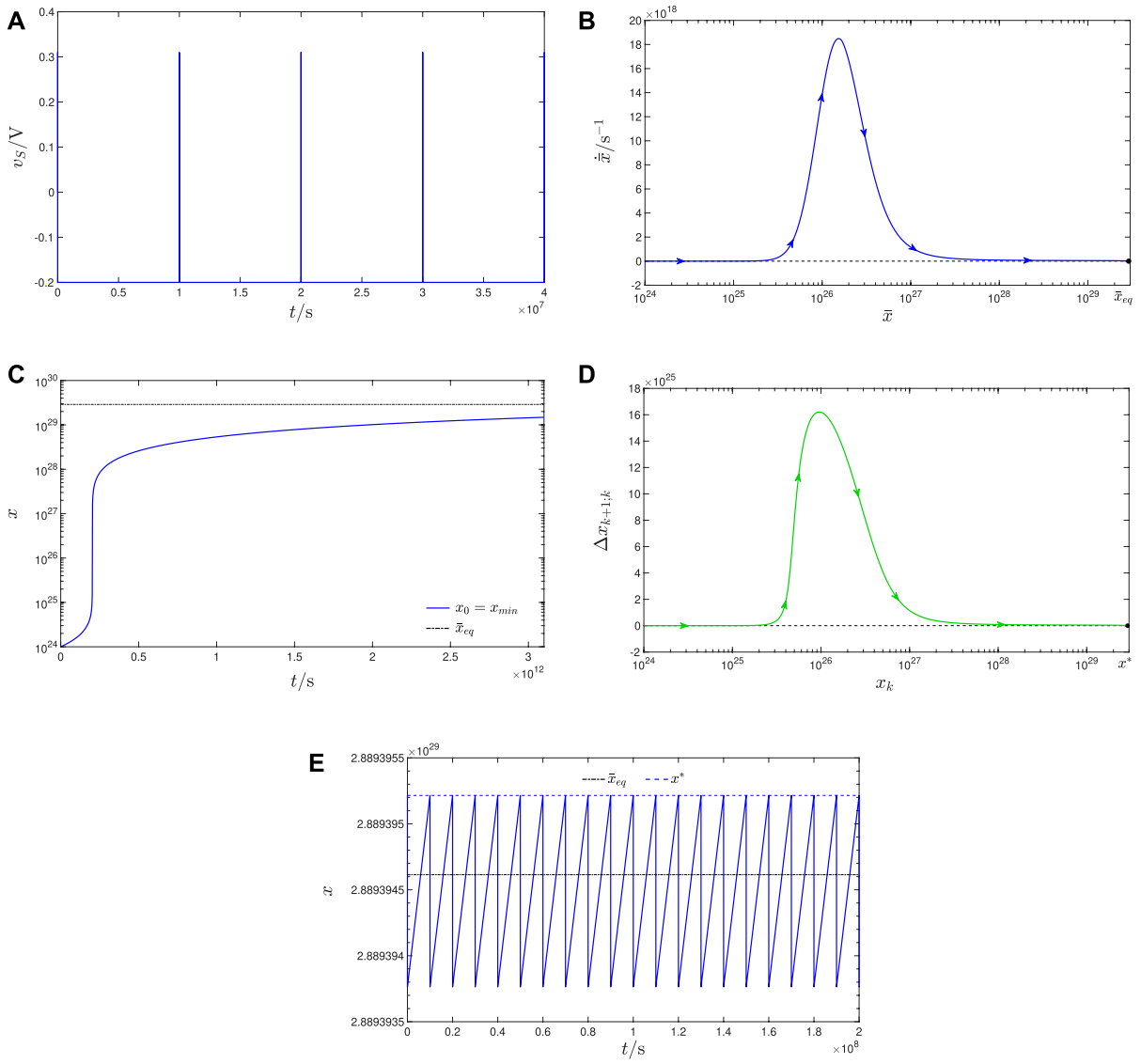

FIGURE 12
(A) Time course of the pulse train-based voltage stimulus v_S, to be applied across the ReRAM cell, manufactured at FZJ, in order to induce monostable oscillatory dynamics around the fully-SET state across its physical medium (case study 1.4). The values for the four parameters, defining its two square pulses per cycle, are $V_+ = +0.31$ V, $\tau_+ = 1 \cdot 10^2$s, $V_- = -0.2$ V, and $\tau_- = 1 \cdot 10^7$s ($T = \tau_+ + \tau_- = 1.00001 \cdot 10^7$s, $r = r_4 = 1 \cdot 10^{-5}$). **(B)** TA-SDR of the TaO_x memristor, under the periodic excitation illustrated in **(A)**. The $\dot{\bar{x}}$ *versus* $\bar{x}$ locus crosses the horizontal axis in one and only one point, revealing the existence of a GAS equilibrium $\bar{x}_{eq}$, lying at $2.8893946 \cdot 10^{29}$, close to yet below the state upper bound $x_{max} = 3 \cdot 10^{29}$ for the respective TA-SE. **(C)** Time evolution of the device memory state x, as recorded in a transient simulation of the test circuit of Figure 2A, under the earlier specified stimulation protocol, from the smallest possible initial condition x_0, chosen as the lower bound x_{min} in the closed set $\mathcal{D}_x$. **(D)** SCPCM of the ReRAM cell in the case study under examination. It reveals the existence of one and only GAS fixed point x^*, located at $2.8893952 \cdot 10^{29}$, for the associated Poincaré map $x_{k+1} = \mathcal{P}(x_k)$. **(E)** Time course of the solution to the periodically forced non-autonomous JART VCM DAE system for $x_0 = x^*$. The memory state settles immediately on a unique oscillation, revolving approximately around the TA-SE equilibrium $\bar{x}_{eq}$, without undergoing a transient dynamical phase. The map fixed point coincides with the maximum of the GAS oscillation in the memory state as the periodic stimulus first excites the OFF dynamics and then the ON dynamics of the device over each cycle.

parameter triplet (V_+, V_-, r). Let us determine the impact of the pulse width ratio r on the number of admissible TA-SE equilibria, given any preliminary choice for the heights V_+ and V_- of the RESET and SET pulses, respectively. Figure 6 provides an exemplary illustration for the dependence of the function $y = \hat{r}(\bar{x}, V_+, V_-)$, expressed by Eq. 14, upon the time-average state $\bar{x}$, for a specific selection of V_+ and V_- (refer to the blue solid trace). The abscissas of the intersections between this curve and the horizontal line $y = r$, associated with a particular choice for the pulse width ratio, correspond to the admissible TA-SE equilibria in this scenario. Clearly, computing the ordinates of the local extrema[11] of the

11 At a local extremum, the derivative of the function $y = \hat{r}(\bar{x}, V_+, V_-)$ with respect to the time average state is null. The local extremum is a local minimum (local maximum) if the second derivative of $y = \hat{r}(\bar{x}, V_+, V_-)$ with respect to the time-average state is positive (negative) therein.

function $y = \hat{r}(\bar{x}, V_+, V_-)$, together with the values it attains when the memory state assumes the bounds in its existence domain, and then sorting this dataset in ascending order, enables partitioning the one-dimensional space, spanned by the parameter r, into a number of regions, each of which includes values, assignable to the pulse width ratio, endowing the resulting TA-SE with a specific number of equilibria. The function, graphed for illustrative purposes in Figure 6, features four local extrema, classifiable either as minima, namely, y_1 and y_2, or as maxima, specifically y_4 and y_5, while it assumes the values y_3 and y_6 at the upper and lower bounds of the memory state existence domain, respectively. These six critical points partition the one-dimensional parameter space into seven regions, specifically[12] $(0, y_1)$, (y_1, y_2), (y_2, y_3), (y_3, y_4), (y_4, y_5), (y_5, y_6), and (y_6, ∞), within which any choice for the pulse width ratio would endow the resulting TA-SE with 0, 2, 4, 5, 3, 1, and 0 equilibria, respectively. Furthermore, it is instructive to note that a crossing between the graphs of the functions $y = \hat{r}(\bar{x}, V_+, V_-)$ and $y = r$ correspond to an asymptotically stable (an unstable) equilibrium for TA-SE if and only if the slope of the curve is negative (positive) therein. A three-equilibrium case study, occurring for a generic choice of the pulse width ratio r, lying within the region (y_4, y_5), is illustrated in Figure 6 as a pedagogical example. Under these circumstances, the solution to the periodically forced ODE (Eq. 1) would exhibit bistability as long as the approximation, inherent to the time averaging method, would not corrupt the accuracy of the predictions, drawn via TA-SDR investigation, which may be verified by means of a SCPCM analysis (Ascoli et al., 2023b). Of course, ultimately, experimental tests shall have to be conducted to verify the emergence of local fading memory effects of this kind in the nano-device.

On the basis of these insights, it is possible to propose a systematic procedure, which, given the heights V_+ and V_- of the RESET and SET pulses, composing the ReRAM cell stimulus over the first τ_+-long and second τ_--long parts of each cycle, respectively, allows determining the number of intersections between the graph of the function $y = \hat{r}(\bar{x}, V_+, V_-)$ and the horizontal line $y = r$, together with the local stability properties of the TA-SE equilibria, corresponding to their abscissas, upon assigning any real value to the pulse width ratio r. The proposed methodology envisages the execution of the following sequence of steps, one after the other, after the preliminary specification[13] of an input pulse height pair (V_+, V_-):

1. Calculate the ordinates of the local extrema of $\hat{r}(\bar{x}, V_+, V_-)$, as well as the values of this function at the endpoints of the memory state existence domain. Sort this dataset of generic cardinality n in ascending order.
2. Given the ith y-value y_i from the resulting tuple $(y_1, y_2, \ldots y_i, \ldots, y_n)$, with $y_1 < y_2 < \ldots < y_i < \ldots < y_n$, compute the parameter Δ_i, denoting the change in the number of intersections between the graph of the function $y = \hat{r}(\bar{x}, V_+, V_-)$ and the horizontal line $y = r$ as r is increased past y_i, for each i value from the set $\{1, 2, \ldots, n\}$. The particular shape of the function $y = \hat{r}(\bar{x}, V_+, V_-)$, which crucially depends upon the preliminary selection of V_+ and V_-, determines the appropriate value, to be assigned to Δ_i, according to the following set of rules:

$$\Delta_i = \begin{cases} +1 & \text{if } y_i \text{ is the value at its left (right) endpoint and its slope is positive (negative) therein,} \\ +2 & \text{if } y_i \text{ is the ordinate of one of its local minima within the bounds of } \mathcal{D}_x, \\ -2 & \text{if } y_i \text{ is the ordinate of one of its local maxima within the bounds of } \mathcal{D}_x, \\ -1 & \text{if } y_i \text{ is the value at its left (right) endpoint and its slope is negative (positive) therein.} \end{cases} \tag{15}$$

3. Focussing finally on the partition of the one-dimensional space, spanned by the parameter r, while the graphs of the functions $\hat{r}(\bar{x}, V_+, V_-)$ and $y = r$ feature no intersection over either of the two regions $(0, y_1)$ and (y_n, ∞), the number of equilibria, which any pulse width ratio, falling within the range (y_j, y_{j+1}), is bound to endow the TA-SE with, may be calculated via $\eta_j = \sum_{i=1}^{i=j} \Delta_i$, for $j \in \{1, 2, \ldots, n-1\}$. If η_j is an even number, then the TA-SE admits $\eta_j/2$ stable equilibria and $\eta_j/2$ unstable equilibria. On the other hand, if η_j is an odd number, then the TA-SE admits $(\eta_j + 1)/2$ $((\eta_j - 1)/2)$ stable equilibria and $(\eta_j - 1)/2$ $((\eta_j + 1)/2)$ unstable equilibria, provided the slope of the function $y = \hat{r}(\bar{x}, V_+, V_-)$ is negative (positive) at its left endpoint.

In the section to follow, the rigorous system-theoretic methodology, based upon the time averaging method, as presented above, shall be applied to the JART VCM model so as to demonstrate its power to predict the correspondence between the choice for the pulse width ratio of the two square pulses, composing the train voltage stimulus over each cycle, and the number of stable asymptotic oscillatory solutions for the periodically forced state equation, upon an exemplary preliminary selection for the pulses' heights.

5 Application of the methodology

In this section, the systematic methodology, proposed in Section 4.3, is applied to an exemplary scenario[14], associated with a particular choice for the pair (V_+, V_-), whose first (second) component specifies the height V_+ (V_-) of the first RESET (second SET) square pulse in the waveform of the AC periodic pulse train voltage stimulus over each cycle. For this scenario, the $\hat{r}(\bar{x}, V_+, V_-)$ *versus* $\bar{x}$ locus is first derived, and four case studies, each of which envisages the assignment of a particular value to the pulse width parameter r, resulting in the existence of a specific number of stable and unstable equilibria for the TA-SE, are discussed. For each case study, numerical simulation results are then presented to validate the

12 The regions $(0, y_1)$ and (y_6, ∞) of the one-dimensional parameter space are uninteresting from a practical viewpoint as they correspond to unaccessible values for the memristor state.

13 An exhaustive numerical exploration of the $V_+ - V_-$ input parameter plane allows to choose RESET and SET input pulse heights so as to obtain a desired shape for the $y = \hat{r}(\bar{x}, V_+, V_-)$ *versus* $\bar{x}$ locus.

14 V_+ (V_-) is intentionally chosen as the amplitude of the positive RESET (negative SET) pulse in each cycle of the asymmetric periodic triangular voltage stimulus adopted to excite the ReRAM cell in the simulation illustrated in Figure 1.

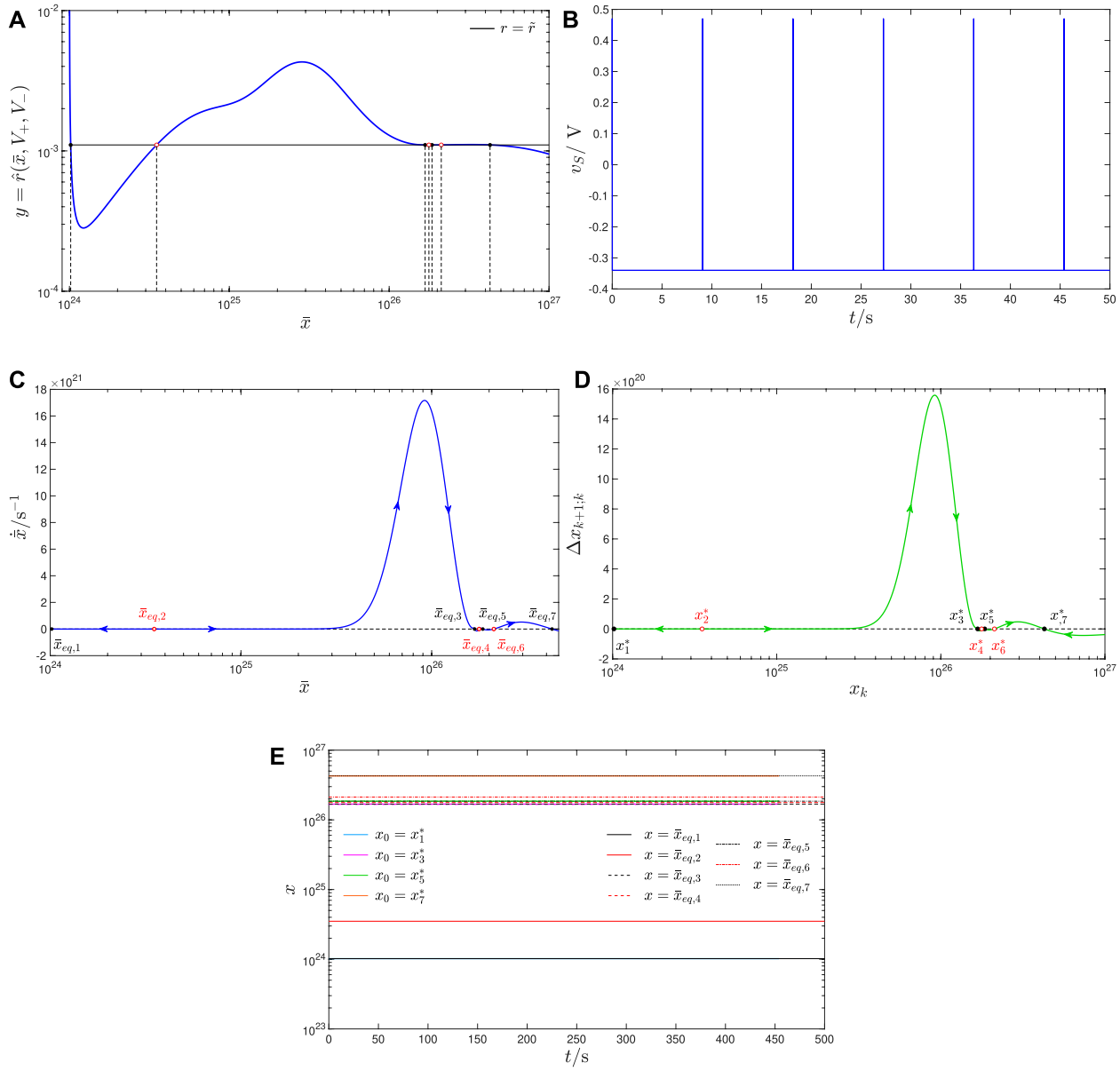

FIGURE 13
(Continued).

accuracy of the system-theoretic predictions, by providing proof of evidence for the emergence of steady-state oscillatory solutions, centred around the stable TA-SE equilibria, for the JART VCM ODE (Eq. 1) subject to the underlying periodic pulse train input.

5.1 Exemplary scenario

Figure 7 shows the dependence of $\hat{r}(\bar{x}, V_+, V_-)$ upon $\bar{x}$ for the input amplitude pair $(V_+, V_-) = (+0.31\ \text{V}, -0.2\ \text{V})$ together with four lines, corresponding to values, assigned to the ordinate y, predicting monostable oscillatory dynamics, involving the lower (r_1) or upper (r_4) memory state bound, bistable periodic operating mode (r_2), and the co-existence of three stable limit cycles in the state space of the first-order periodically forced continuous-time system (r_3), respectively. Each of these cases studies shall be analysed in depth below.

5.1.1 Case study 1.1: monostable oscillatory response around the fully-RESET state

Choosing $r = r_1 = 1$ (refer to the horizontal black line in Figure 7), the proposed system-theoretic method predicts a unique oscillatory operating mode around the fully-RESET state for the TaO_x ReRAM cell manufactured at FZJ. Assigning the common value of $10 \cdot 10^3$s to both τ_- and τ_+, the resulting periodic voltage stimulus v_S, applied across the memristor, is shown in plot (a) of Figure 8. Here, the TA-SDR predicts a single globally asymptotically stable (GAS) oscillatory solution for the device memory state, as depicted in plot (b) of the same figure. As, in this case study, the only equilibrium $\bar{x}_{eq}$ for the TA-SE is very close to yet larger than $x_{\min} = 1 \cdot 10^{+24}$, the memristor state, initiated from its

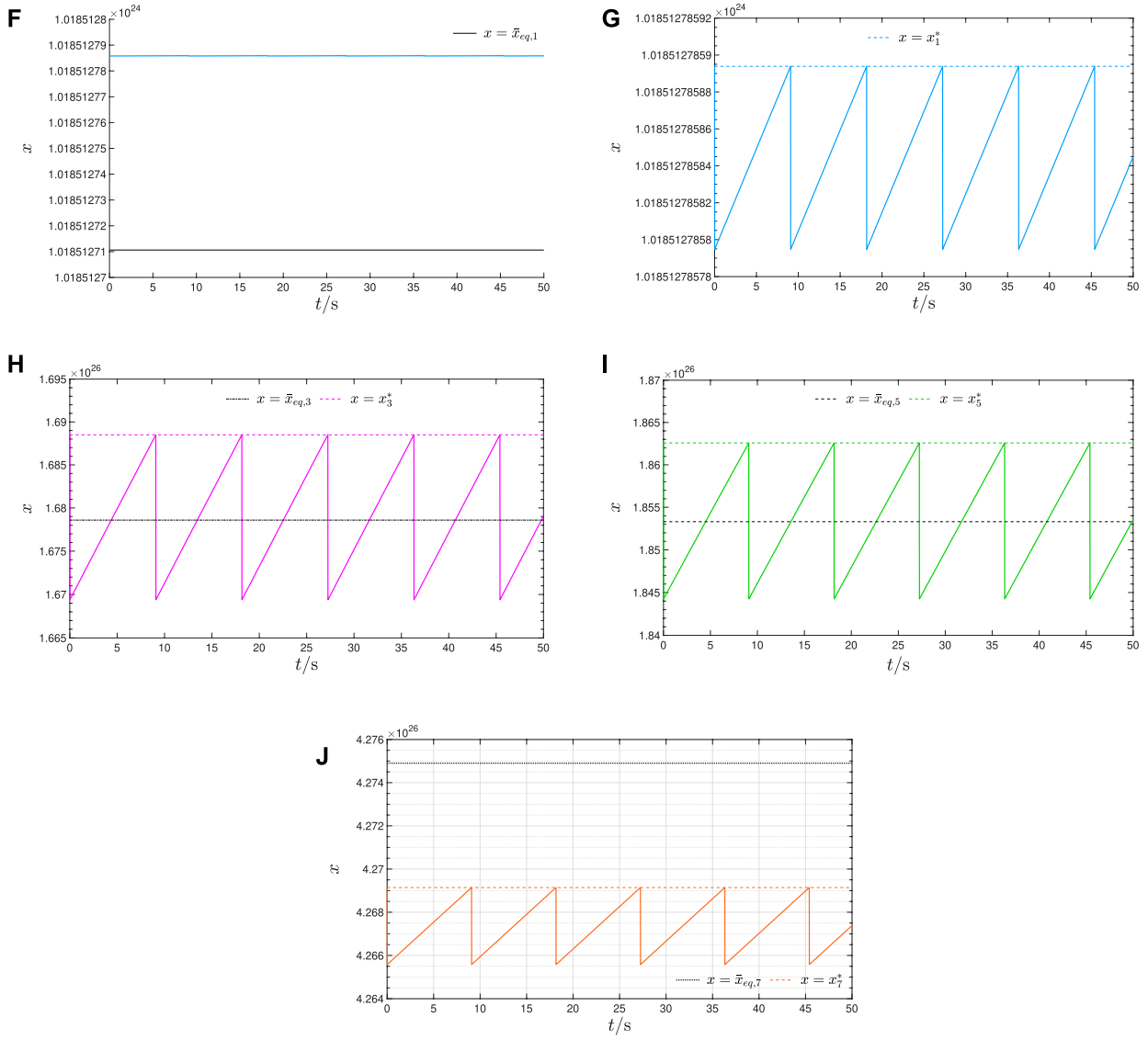

FIGURE 13
(Continued). Coexistence of four stable oscillatory operating modes for the periodically-forced ReRAM cell under a different selection of the pulse height parameter pair and suitable pulse width ratio. **(A)** Blue trace: locus of $\hat{r}(\bar{x}, V_+, V_-)$ *versus* $\bar{x}$, as descending from Eq. 14, for $(V_+, V_-) = (+0.47\ \mathrm{V}, -0.34\ \mathrm{V})$. Seven are the crossings between the blue trace and the black horizontal line $y = \bar{r} = 1.1 \cdot 10^{-3}$. Their abscissas, specifically $\bar{x}_{eq,1} = 1.018512710613 \cdot 10^{24}$, $\bar{x}_{eq,2} = 3.509814043557 \cdot 10^{24}$, $\bar{x}_{eq,3} = 1.678591472274 \cdot 10^{26}$, $\bar{x}_{eq,4} = 1.772425971677 \cdot 10^{26}$, $\bar{x}_{eq,5} = 1.853306020949 \cdot 10^{26}$, $\bar{x}_{eq,6} = 2.11774636839 \cdot 10^{26}$, and $\bar{x}_{eq,7} = 4.27490164355 \cdot 10^{26}$, constitute the equilibria of the TA-SE adapted to the case study under focus. **(B)** Time waveform of a two-pulse-per-cycle train voltage signal v_S from the class identified by the predefined input parameter triplet (V_+, V_-, r). The width τ_+ (τ_-) for the first (second) RESET (SET) pulse in each cycle is here set to $\tau_+ = 1 \cdot 10^{-2}$s ($\tau_- = 9.07$ s). The input period T is then 9.08s. **(C)** TA-SDR of the JART VCM ODE under the above specified AC periodic excitation voltage signal. The zeros of the time average state evolution function, forming the right hand side of the TA-SE (Eq. 7), coincide with the crossings between the blue trace and black horizontal line in plot **(A)**. **(D)** SCPCM of the periodically-forced memristive ODE system. The abscissas of the intersections between the $\Delta x_{k+1;k}$ *versus* x_k locus and the horizontal axis, representing the fixed points of the Poincaré map, are $x_1^* = 1.018512785894 \cdot 10^{24}$, $x_2^* = 3.509815501129 \cdot 10^{24}$, $x_3^* = 1.688496847014 \cdot 10^{26}$, $x_4^* = 1.781514349068 \cdot 10^{26}$, $x_5^* = 1.862577512645 \cdot 10^{26}$, $x_6^* = 2.125872843063 \cdot 10^{26}$, and $x_7^* = 4.269140935744 \cdot 10^{26}$. **(E)** Time course of the solution to the JART VCM ODE, resulting by enforcing its input v to follow the pulse train voltage stimulus v_S in **(A)**, from each initial condition in the set $S_3 \triangleq \{x_{0,1}, x_{0,2}, x_{0,3}, x_{0,4}\} = \{x_1^*, x_3^*, x_5^*, x_7^*\}$. **(F)** and **(G–J)** Close-up view of the oscillatory solution, illustrated in **(E)**, and initiated from the first, second, third, and fourth initial conditions in S_3.

highest admissible value $x_0 = x_{\max} = 3 \cdot 10^{29}$, progressively descends toward the lower bound in its existence domain $\mathcal{D}_x$ (see Figure 8C). Indeed, after transients decay to zero, the oscillatory waveform of the memory state is found to revolve precisely around the mean value, predicted by the TA-SDR analysis, i.e., $\bar{x}_{eq} = 1.000015603 \cdot 10^{+24}$, as illustrated in plot (d) of the same figure.

5.1.2 Case study 1.2: coexistence of two stable oscillatory operating modes, one of which is around the fully-RESET state

In Figure 1A, a triangular periodic voltage waveform was employed to stimulate the ReRAM cell so as to endow it with oscillatory bistability, similarly as first reported in (Ascoli et al.,

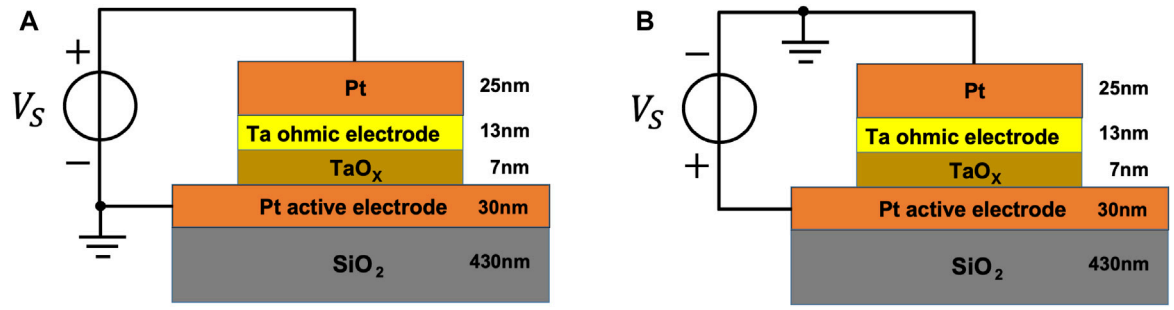

FIGURE 14
(A) Qualitative sketch of the device physical stack, illustrating how a voltage stimulus v_S was applied between its terminals for the bistability test in the laboratory. **(B)** Illustration of the assumption, made for the theoretical analysis presented in the paper, on the way a voltage source v_S is connected across the ReRAM cell for inducing nonlinear phenomena across its physical medium (see also Supplementary Figure 20).

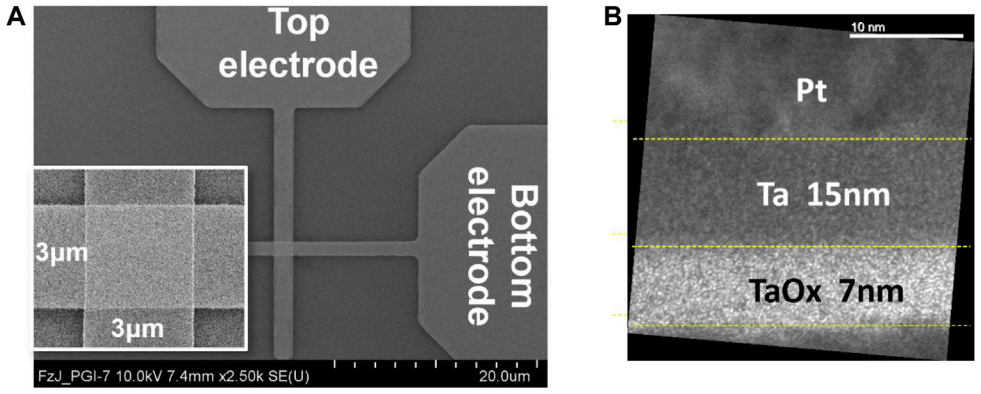

FIGURE 15
(A) Top-view SEM image of a VCM crosspoint device of the junction area 3 × 3 μm^2. **(B)** Cross-sectional TEM image of a ReRAM cell of this kind, revealing the thickness of each layer in its physical stack (Ascoli et al., 2022).

2022), where, however, no theoretical analysis was provided to explain the coexistence of two periodic solutions, one of which affected by the RESET boundary condition, for the memory state. In this case study, the system-theoretic method, described in Section 3, is employed to shape a square wave voltage stimulus in such a way to induce a similar nonlinear dynamic phenomenon in the device. In particular, keeping the positive (negative) height V_+ (V_-) of the first (second) pulse in each cycle of the input voltage train unaltered relative to case study 1.1, this may be achieved by setting the RESET-to-SET pulse width ratio r to $r_2 = 1.5 \cdot 10^{-2}$, as may be inferred by inspecting the number of crossings between the violet horizontal line and the blue curve in Figure 7, as well as the slope of the latter trace at each of their locations. Figure 9A shows a periodic voltage stimulus, satisfying these constraints, for $\tau_+ = 1 \cdot 10^4$s and $\tau_- = 6.667 \cdot 10^5$s. Under this periodic excitation, the TA-SE of the ReRAM cell admits three equilibria, specifically $\bar{x}_{eq,1} = 1.00105 \cdot 10^{24}$, $\bar{x}_{eq,2} = 8.93240 \cdot 10^{24}$, and $\bar{x}_{eq,3} = 5.84158 \cdot 10^{25}$, of which the outer ones (the inner one) are locally stable (is unstable). These equilibria coincide with the points of intersection between the line $y = r_2$ and the $\hat{r}(\bar{x}, V_+, V_-)$ *versus* $\bar{x}$ locus for (V_+, V_-) = (0.31 V, −0.2 V) in Figure 7.

Plots (c), (e), and (g) of Figure 9, respectively, show the time evolution of the memory state, as recorded from transient simulations of the DAE set (Eqs 1, 2), extracted numerically from the JART VCM model, as described in Supplementary Appendix A.1, covering a time span of 70,000, 14,000, and 70,000 cycles, respectively, and resulting upon fixing preliminarily the initial memristor state x_0 to the first, second, and third values from the set $S_1 = \{x_{0,1}, x_{0,2}, x_{0,3}\} = \{8 \cdot 10^{24}, 1 \cdot 10^{25}, 3 \cdot 10^{29}\}$. With reference to Figure 9C, the solution of the JART VCM DAE set, starting off from the first initial condition in S_1, descends progressively toward a steady-state oscillatory waveform, which is found to revolve around the leftmost locally stable TA-SE equilibrium $\bar{x}_{eq,1}$, as shown in plot (d). On the other hand, evolving from the second (third) initial condition in the above specified set, the memory state solution, depicted in plot (e) ((g)), approaches asymptotically from below (from above) an oscillation, which is centred around the rightmost locally stable TA-SE equilibrium $\bar{x}_{eq,3}$, as observable in plot (f) ((h)). Figure 9I depicts the SCPCM, extracted from the Poincaré map of the periodically forced memristive system, which confirms the accuracy of the predictions drawn via TA-SDR analysis, by showing how the

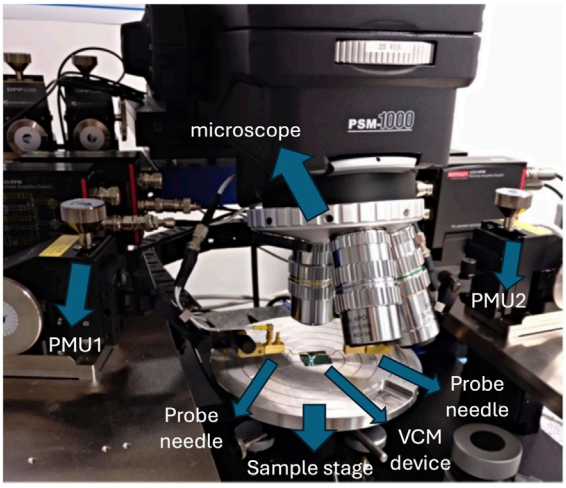

FIGURE 16
Probe station, including microscope, sample stage, and probe needles. Two pulse measurement units (PMUs), indicated here as PMU1 and PMU2, are also visible in the background.

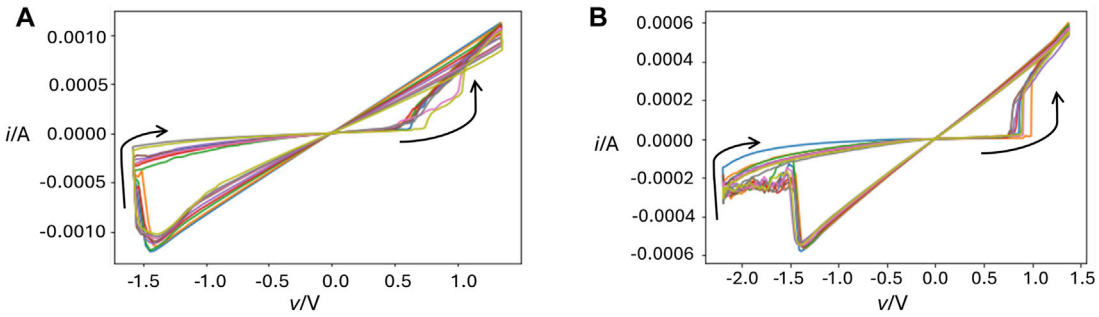

FIGURE 17
Current *i versus* voltage *v* loci of the ReRAM device as an asymmetric triangular voltage signal v_S at frequency 1 kHz is let to fall between its terminals for 10 consecutive input cycles. The amplitude $\hat{v}_{SET}$ of the positive triangular pulse was fixed to 1.4 V, whereas the amplitude $\hat{v}_{RESET}$ of the negative triangular pulse was modulated to program different resistances into the VCM cell. The loci in **(A, B)** were recorded when $\hat{v}_{RESET}$ was set to −1.6 V (−2.2 V). As Joule heating-related positive feedback mechanisms may lead to an uncontrollable upsurge in the device current, the latter is constrained to keep below or at most equal to a compliance level I_{cc} of 1.2 mA.

train voltage stimulus from plot (a) of the same figure endows the device with two oscillatory operating modes. Given that the RESET pulse precedes the SET pulse in each period of the two-pulse-per-cycle input train, the first (third) locally stable fixed point x_1^* (x_3^*) of the map, located at $1.00105 \cdot 10^{24}$ ($5.97593 \cdot 10^{25}$), coincides with the maximum of the steady-state oscillation in plot (d) (in either plots (f) and (h)). Last but not least, as may be inferred from plots (J), (K), and (L), computing the running time average of the time series $x(t)$, resulting from the numerical simulation of the SE (Eq. 1), adapted to the JART VCM model, for the first, second, and third initial conditions in the set S_1, respectively, it is found to match from $t = T$ the respective theoretical prediction, obtained as solution $\bar{x}(t)$ to the TA-SE (7), adapted to the same model, when the initial condition $\bar{x}_0$ is computed through the formula (Eq. 3) from the first cycle of the solution $x(t)$ to the SE shown in turn in plots (c), (e), and (g).

5.1.3 Case study 1.3: coexistence of three stable oscillatory operating modes, one of which is around the fully-RESET state

The brown horizontal line $y = r_3 = 2.3 \cdot 10^{-3}$ from Figure 7 meets the locus of $\hat{r}(\bar{x}, V_+, V_-)$ *versus* $\bar{x}$, resulting from assigning +0.31 V and −0.2 V to V_+ and V_-, respectively, in five locations. Among the stable ones, marked with black filled circles, two of them lie well within the memory state existence domain $\mathcal{D}_x$. In fact, as revealed shortly, in this case study, after transients vanish, the periodically driven JART VCM ODE may admit one of three locally stable periodic solutions, depending upon the initial condition, while boundary conditions affect only one of them. A pulse train voltage signal, composed over each cycle of one positive RESET and one negative SET pulse, appearing in this order and featuring height–width parameter pair $(V_+, \tau_+) = (+0.31\ \text{V}, 10 \cdot 10^3\text{s})$ and $(V_-, \tau_-) = (-0.2\ \text{V}, 4.385 \cdot 10^6\text{s})$, respectively, which satisfies the

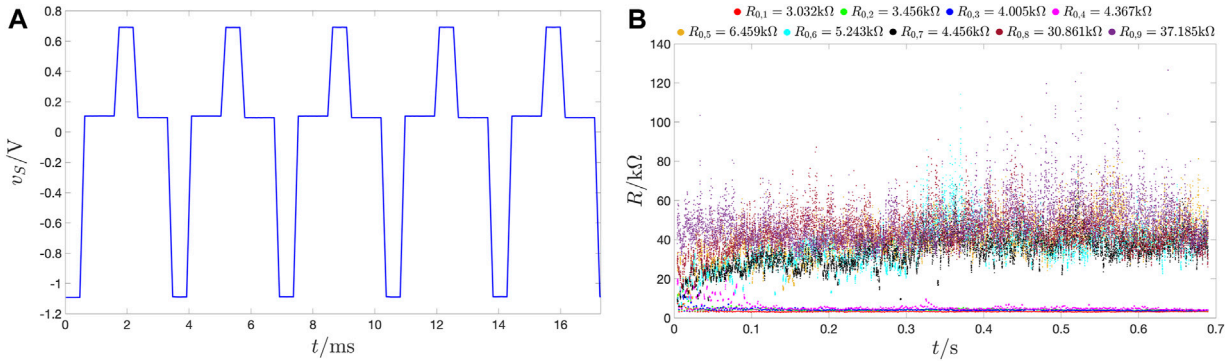

FIGURE 18
(A) Time course of the four-pulse-per-cycle train voltage stimulus v_S, let to fall across a VCM device sample in the laboratory, as measured over the first five periods. **(B)** Transient evolution of the device resistance, sampled at 20 regularly spaced time instants after each RESET or SET writes pulse, toward a lower (an upper) locally stable steady-state oscillatory solution from any of the first four (last five) initial conditions from the set $S_{3,R} \triangleq \{R_{0,1}, R_{0,2}, R_{0,3}, R_{0,4}, R_{0,5}, R_{0,6}, R_{0,7}, R_{0,8}, R_{0,9}\} = \{3.032, 3.456, 4.005, 4.367, 6.459, 5.243, 4.456, 30.861, 37.185\}\text{k}\Omega$, as recorded from the 2nd to the 200th input period. As a result, the initial condition, separating the basins of attraction of the two admissible locally stable oscillatory solutions for the resistance R at steady state, lies between $R_{0,4} = 4.367$ kΩ and $R_{0,7} = 4.456$ kΩ.

constraint $r = r_3$, is applied across the ReRAM cell, described via the JART VCM DAE set model (Bengel et al., 2022), in the test circuit of Figure 2A, as shown in plot (a) of Figure 10. Plot (b) of the same figure depicts the TA-SDR of the ReRAM cell associated with this AC periodic stimulus. It reveals that, as expected, in these circumstances, the TA-SE (7) admits three locally stable equilibria at the very same locations corresponding to the three points, at which the blue locus crosses the brown horizontal trace with a negative slope in Figure 7. Transient simulations of the test circuit demonstrate the accuracy of the predictions drawn through TA-SDR analysis. Figure 10C shows the transitory behaviour of the memory state of the periodically forced ReRAM cell from each initial condition x_0 in the set $S_2 \triangleq \{x_{0,1}, x_{0,2}, x_{0,3}, x_{0,4}, x_{0,5}\} = \{1.9 \cdot 10^{24}, 4.6 \cdot 10^{25}, 3.5 \cdot 10^{26}, 7.5 \cdot 10^{26}, 7.4 \cdot 10^{28}\}$ over a $1 \cdot 10^9$s-long time span. Due to the complex slow–fast dynamics of the ReRAM cell (Ascoli et al., 2022), whose response to stimuli may, in general, evolve along time scales, spanning a multi-decade range, depending upon initial condition and excitation strength, the ODE solution attains a steady state within time intervals, differing by orders of magnitude, for the first, second or third, and fourth or fifth initial conditions in the earlier specified set S_2, calling for the use of specific graphs, namely, Figures 11A, C, E, respectively, for a better visualization of the respective transients. Depending upon the initial condition x_0, the memory state of the periodically driven memristor may asymptotically evolve along either of three admissible oscillatory waveforms, revolving around levels, approximately equal to $\bar{x}_{eq,1}$, $\bar{x}_{eq,3}$, and $\bar{x}_{eq,5}$, as illustrated in turn in Figures 11B, D, F. Remarkably, as illustrated in plot (c) ((e)) of this figure, the ODE solutions, initiated from the second and third (the fourth and fifth) initial conditions in the aforementioned set, approach, from below and from above, respectively, the inner (top-most) oscillatory solution, whose excursion is clearly affected neither by the lower $x_{\min} = 1 \cdot 10^{24}$ nor by the upper $x_{\max} = 3 \cdot 10^{29}$ bound in the state existence domain $\mathcal{D}_x$.

Supplementary Appendix A.2 reports the promising results of initial investigations aimed to define an appropriate setup for a future experimental verification of tri-stability in the oscillatory device via pulse generators with physical limitations.

5.1.4 Case study 1.4: monostable oscillatory response around the fully-SET state

Setting r to $r_4 = 1 \cdot 10^{-5}$ (see the green horizontal line in Figure 7), the memristor is expected to lock into a unique oscillatory operating mode around the fully-SET state. Indeed, this is the case. Keeping the positive (negative) height V_+ (V_-) of the first (second) RESET (SET) pulse in each cycle of the input train, as specified in all the case studies in the exemplary scenario, Figure 7 refers to, and setting its temporal width τ_+ (τ_-) to 10^2s (10^5s), which meets the requirement on r, results in the voltage stimulus, illustrated in Figure 12A. Here, the TA-SE (Eq. 7) admits one and only one equilibrium $\bar{x}_{eq}$, located close to, but below, the highest possible memristor state value $x_{\max}$, precisely at $2.8893946 \cdot 10^{29}$, as demonstrated in plot (b) of the same figure, visualising the TA-SDR of the periodically driven ReRAM cell in the case study under focus. As revealed in Figure 12C, showing the time course of the memory state, initiated from its lowest possible value $x_{\min}$, as resulting from a numerical integration of the JART VCM DAE set under the above specified periodic excitation, the device experiences very long transients before settling on a GAS oscillatory operating mode around its fully-SET state. The powerful SCPCM technique may be employed to acquire in a straightforward and time-efficient way the time waveform, along which the memory state would be found to evolve, after transients vanish. In fact, setting the initial condition for a generic first-order ODE system, subject to a certain periodic input, to a stable fixed point of the associated Poincaré map, the respective numerical solution evolves directly along one of its admissible steady-state oscillatory waveforms, without experiencing a preliminary transient phase. Plot (d) of Figure 12 shows the SCPCM of the periodically forced ReRAM cell in the case study under

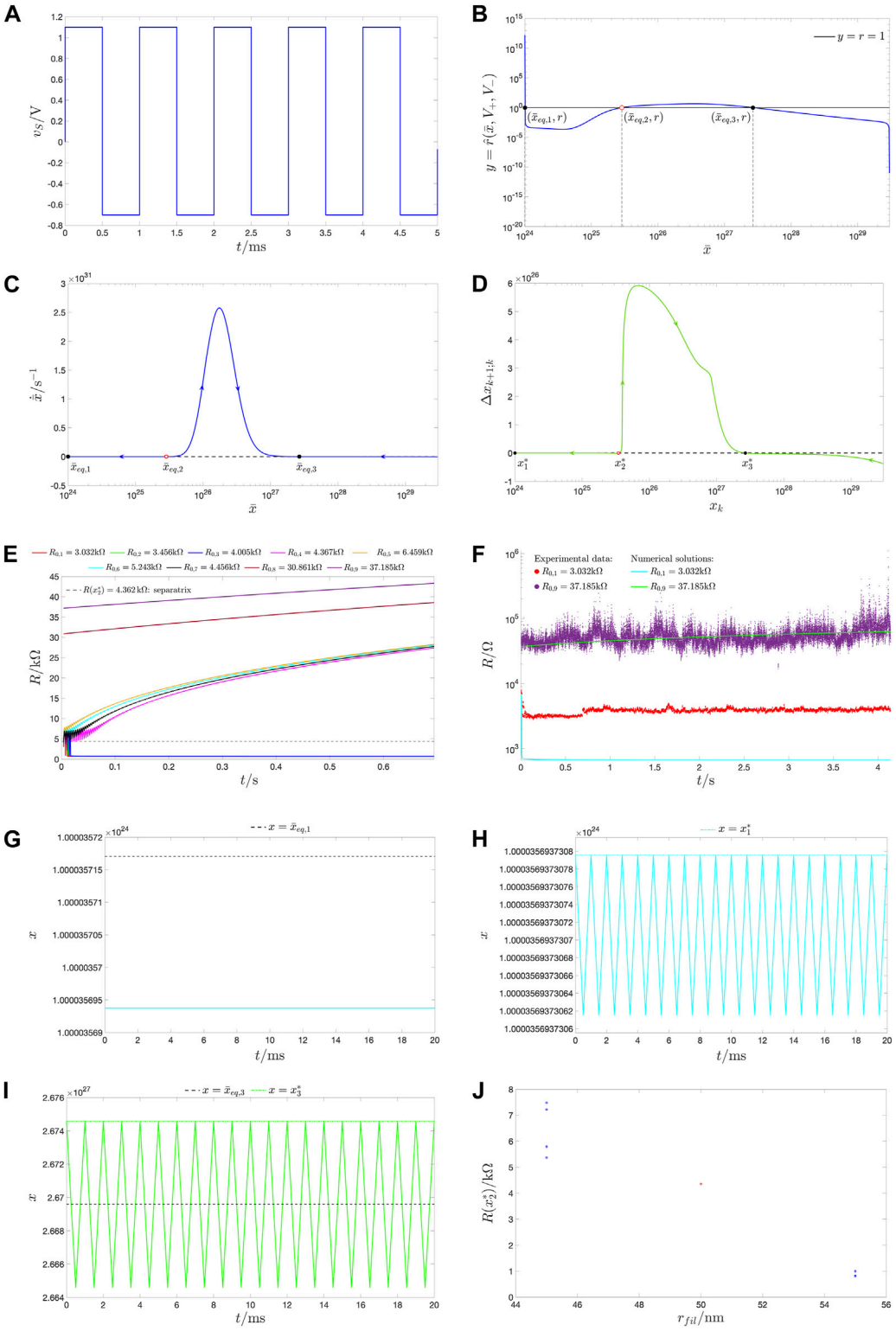

FIGURE 19
(A) Time waveform of a two-pulse-per-cycle train voltage stimulus v_S, used as the memristor voltage v in the numerical simulation of the JART VCM v1 model for reproducing qualitatively the experimental observations, across the first five periods. The amplitude V_+ (V_-) of the first (second) RESET (SET) pulse in each cycle is chosen as 1.1 V (−0.7 V). The RESET and SET pulse widths, respectively, referred to as τ_+ and τ_-, are assumed to be identical and set to 0.5 ms each. **(B)** Graph of $\hat{r}(\bar{x}, V_+, V_-)$ as a function of $\bar{x}$ for $(V_+, V_-) = (1.1\ \mathrm{V}, -0.7\ \mathrm{V})$. Its four intersections with the black solid horizontal line $y = r = 1$ represent the equilibria of the TA-SE (Eq. 7) for the specified input parameter triplet (V_+, V_-, r). The TA-SE equilibria lie at $\bar{x}_{eq,1} = 1.00003571706985 \cdot 10^{24}$, $\bar{x}_{eq,2} = 2.86242953188943 \cdot 10^{25}$, and $\bar{x}_{eq,3} = 2.6695910284688 \cdot 10^{27}$. The outer ones (The inner one) are (is) locally asymptotically stable (unstable), predicting a bistable oscillatory behaviour for the periodically driven ReRAM cell. **(C)** TA-SDR associated with the JART VCM v1 model subject to a two-

(*Continued*)

FIGURE 19 (Continued)
pulse-per-cycle train voltage input characterised by the aforementioned parameter triplet. **(D)** SCPCM extracted from the JART VCM v1 model subject to the particular pulse train in plot **(C)**. The fixed points of the Poincaré map $x_{k+1} = \mathcal{P}(x_k)$ lie at $x_1^* = 1.0000356937308 \cdot 10^{24}$, $x_2^* = 3.46292363939077 \cdot 10^{25}$, and $x_3^* = 2.67457600665113 \cdot 10^{27}$, of which the first and third ones (the second one) are (is) locally asymptotically stable (unstable). **(E)** Solutions of the JART VCM model expressed in terms of the device resistance R, computed from the memory state x for a read voltage V of 0.1 V, from each initial condition in the set $S_{3,R}$ specified in the caption of Figure 18, for the particular non-autonomous case, where v is enforced to follow v_S from plot **(C)** at all times. As indicated through a dashed horizontal grey line, the initial condition, which separates the basins of attraction of the two oscillatory steady states, is $R(x_2^*) = 4.362\text{k}\Omega$, which is 5Ω off the range (4.367 kΩ, 4.456 kΩ), where the separatrix was found to lie in the experiments. It follows that, unlike what was the case in the measurements of Figure 18B, here, the pink trace, started off from the initial condition $R_{0,4} = 4.367$ kΩ, approaches the upper steady-state oscillation. The time evolution of each of the other traces agrees with the corresponding experimental measurement. **(F)** Qualitative agreement between experiments and JART VCM v1 model simulations in recording the time behaviour of the device resistance R in response to the pulse train voltage stimulus, shaped as shown in Figure 18A and plot **(A)** of this figure in the laboratory measurements and in the DAE set numerical integrations, respectively, from two initial conditions, specifically $R_{0,1} = 3.032$ kΩ and $R_{0,9} = 37.185$ kΩ, belonging to the set $S_{3,R}$. **(G, H)** Numerical solution to the JART VCM v1 model for $x_0 = x_1^*$ over time, including the TA-SE equilibrium $\bar{x}_{eq,1}$ (Poincaré map fixed point x_1^*). The time waveform of the device memory state revolves around the lower steady-state oscillation from $t = 0$. **(I)** Time course of the device memory state from $x_0 = x_3^*$ together with the TA-SE equilibrium $\bar{x}_{eq,3}$ and the Poincaré map fixed point x_3^*. Once again, the device state undergoes no transient, exhibiting the upper steady-state oscillatory waveform straight away from the beginning of the simulation. In plot **(H, I)**, as expected, the first (third) map fixed point coincides with the maximum of the lower (upper) steady-state oscillation in the memory state (Ascoli et al., 2023b). **(J)** Blue circle markers: spread in the values of the separatrix point x_2^*, expressed in terms of the device resistance $R(x_2^*)$, evaluated at the read voltage $V = -0.1$ V, upon any possible combination of values, assigned to five particular model parameters of critical impact on the device-to-device variability (Bengel et al., 2020), specifically r_{fil}, l_{cell}, l_{disc}, x_{min}, and x_{max}, and sampled from a set of cardinality 2, including two extremes, i.e., −10% and +10%, of the respective nominal levels from Supplementary Table A1, as a function of the filament radius, which was found to have the most significant correlation with the location of the second fixed point of the Poincaré map. The red circle marker provides a reference point $(r_{\text{fil}}, R(x_2^*)) = (50\text{nm}, 4.362\text{k}\Omega)$, being associated with the nominal case. Importantly, r_{fil} values lower (larger) than the nominal level map into $R(x_2^*)$ values above (below) the ordinate of the red marker, providing evidence for the relation of inverse proportionality linking $R(x_2^*)$ and r_{fil}.

examination. Setting the initial condition x_0 for the memristor state in the test circuit of Figure 2A to the only fixed point $x^\star$ of the map, lying at $2.8893952 \cdot 10^{29}$, the memristor locks into a unique oscillatory mode, around its fully-SET state, from the beginning of the simulation, as illustrated in Figure 12E. Moreover, as expected, the map fixed point identifies the maximum of the GAS oscillatory solution for the memory state.

6 Uncovering novel forms of device multimodal oscillatory dynamics via input pulse height parameter modulation

The exploration of other regions of the V_+-V_- input parameter plane revealed how wider the spectrum of oscillatory dynamics inducible in the ReRAM cell is upon pulse train stimulation. In fact, the choice of a certain pulse height parameter pair sets the periodically driven JART VCM DAE set on a given invariant manifold, characterised by distinctive oscillatory dynamics alternating one after the other via bifurcation phenomena upon pulse width ratio modulation. To name but one example[15], this section explains how one may massage the pulse train properties so as to trigger the coexistence of four locally stable oscillatory solutions for the ReRAM cell memory state. Assigning +0.47 V (−0.34 V) to the RESET (SET) pulse height V_+ (V_-), the locus of the function $y = \hat{r}(\bar{x}, V_+, V_-)$ *versus* the time-average state $\bar{x}$ appears as shown through a blue trace in Figure 13A. The black horizontal line $y = \tilde{r} = 1.1 \cdot 10^{-3}$ intersects this locus as many as seven times. The abscissas of the crossings, corresponding to the equilibria, which the TA-SE (Eq. 7) admits in this case study, are $\bar{x}_{eq,1} = 1.018512710613 \cdot 10^{24}$, $\bar{x}_{eq,2} = 3.509814043557 \cdot 10^{24}$, $\bar{x}_{eq,3} = 1.678591472274 \cdot 10^{26}$, $\bar{x}_{eq,4} = 1.772425971677 \cdot 10^{26}$, $\bar{x}_{eq,5} = 1.853306020949 \cdot 10^{26}$, $\bar{x}_{eq,6} = 2.11774636839 \cdot 10^{26}$, and $\bar{x}_{eq,7} = 4.27490164355 \cdot 10^{26}$. The TA-SE equilibria, endowed with an even (odd) number label, are unstable (locally stable). Setting the RESET (SET) pulse width τ_+ (τ_-) to 10 ms (9.07 s), Figure 13B depicts a square wave voltage signal v_S from the class associated with the input parameter triplet $(V_+, V_-, r) = (+0.47\text{ V}, -0.34\text{ V}, 1.1 \cdot 10^{-3})$. Figure 13C shows the directed $\dot{\bar{x}}$ *versus* $\bar{x}$ locus, predicting the coexistence of four locally asymptotically stable oscillatory solutions for the state of the ReRAM cell subject to the pulse train voltage stimulus from plot (a) of the same figure. The directed $\Delta x_{k;k+1}$ versus x_k locus, confirming the accuracy of the TA-SDR predictions, is presented in Figure 13D. It reveals the existence of seven fixed points for the Poincaré map, specifically $x_1^\star = 1.018512785894 \cdot 10^{24}$, $x_2^\star = 3.509815501129 \cdot 10^{24}$, $x_3^\star = 1.688496847014 \cdot 10^{26}$, $x_4^\star = 1.781514349068 \cdot 10^{26}$, $x_5^\star = 1.862577512645 \cdot 10^{26}$, $x_6^\star = 2.125872843063 \cdot 10^{26}$, and $x_7^\star = 4.269140935744 \cdot 10^{26}$. Figure 13E depicts the time course of the solution to the ODE (Eq. 1) from each initial condition x_0 from the set $S_3 \triangleq \{x_{0,1}, x_{0,2}, x_{0,3}, x_{0,4}\} = \{x_1^\star, x_3^\star, x_5^\star, x_7^\star\}$, including the stable fixed points of the Poincaré map. As expected, the solutions directly lock into the respective steady states, experiencing no transient effects (the seven TA-SE equilibria are also reported in this figure to demonstrate the accuracy of the TA-SDR analysis). Clearly, in this case study, the ReRAM cell state concurrently admits four distinct oscillatory solutions. A zoom-in view of the oscillation in the state, extracted from Figure 13E for the first, second, third, and fourth initial conditions from the aforementioned set, is, respectively, visualised in plot (f) and [16] (g), (h), (i), and (j) of the same figure. The TA-SE equilibrium lies outside of the oscillation for the first (fourth) solution, as shown in plot (f) ((j)). However, the relative error for the ith solution

15 As a further example, by appropriate choice for the input parameters, it is also possible to endow the memristor with one and only one oscillatory operating mode, envisaging a swing for its resistance well-confined within the allowable range. As the main focus of this research paper is to explore multistability in the oscillatory response of the periodically pulse-driven ReRAM cell, the analysis of a case study of this kind is omitted from the investigations.

x_i, computed as $e_i \triangleq (\bar{x}_{eq,i} - \bar{x}_{i,0})/\bar{x}_{i,0}$, where $\bar{x}_{i,0}$ denotes the mean value of the ith solution itself, evaluated arbitrarily over the first input cycle according to Eq. 3, is found to be rather small for each i value in {1, 2, 3, 4}, particularly $\bar{x}_{1,0} = 1.0185 \cdot 10^{24}$, $\bar{x}_{2,0} = 1.6789 \cdot 10^{26}$, $\bar{x}_{3,0} = 1.8534 \cdot 10^{26}$, and $\bar{x}_{4,0} = 4.2674 \cdot 10^{26}$, yielding $e_1 = -7.3863 \cdot 10^{-8}$, $e_2 = -2.1018 \cdot 10^{-4}$, $e_3 = -6.3329 \cdot 10^{-5}$, and $e_4 = 1.7669 \cdot 10^{-3}$. In each case, the initial condition also coincides with the maximum of the oscillation, as expected from the Poincaré map analysis, which, given its higher accuracy relative to the TA-SDR technique, should always be employed to verify the predictions drawn by means of the time averaging method (Ascoli et al., 2023b). As a concluding remark, this section has shown how exploring the V_+–V_- parameter plane is possible to craft pulse train stimuli, which trigger the emergence of various different multimodal oscillatory phenomena in the ReRAM cell, which shows once more the richness of the nonlinear dynamics of a memristive physical realization of this kind.

Remark 2. In view of a future experimental validation of the theory, toward a potential exploitation of the multistable oscillatory response of the periodically driven nano-device for electronics applications, the intrinsic physical limitations in the laboratory instrumentation tools should be considered. The minimum allowable rise/fall time for a square pulse, emitted by any of the AC periodic voltage sources, employable in our laboratories for generating a two-pulse-per cycle train voltage stimulus, is mandatorily 10^{-4} times the maximum between the widths of the SET and RESET pulses in the input waveform over each cycle. Since the narrower pulse width need to be at least one order of magnitude larger than the minimum allowable pulse rise/fall time, this directly sets a soft constraint on the upper bound for the pulse width ratio, which is allowed to range approximately within the limited value set, expressed here:

$$r \in \left(1 \cdot 10^{-3}, 1 \cdot 10^{+3}\right). \tag{16}$$

Initial investigations, aimed to craft ReRAM cell stimuli, which roughly comply with the restrictive condition (Eq. 16), have already delivered promising results, as revealed in Supplementary Appendix A.2, as well as in Section 6.

The study, described in this section, was a source of inspiration for setting up an *ad hoc* experiment, enabling to record the bistable oscillatory behaviour of the VCM device under suitable periodic pulse train stimulation in the laboratory, as reported, for the first time ever in the literature, in the remainder of the main text of our manuscript.

7 Experimental evidence for bistability

7.1 Device stack

The TaO_x valence change memory (VCM) device, subject to the experimental test for bistability, was fabricated at the facilities of Forschungszentrum Jülich (FZJ). As shown in either plot of Figure 14, the ReRAM cell consists of a metal–insulator–metal (MIM) physical stack, where a 7-nm-thick tantalum oxide (TaOx) layer is sandwiched between a 30-nm-thick Pt layer, playing the role of the top active electrode, and sitting on top of a 430-nm-thick SiO_2 substrate, and a 13-nm-thick tantalum (Ta) layer, acting as the bottom ohmic electrode, and covered by yet another 25-nm-thick Pt capping layer. Plot (a) of Figure 14 shows how voltage stimuli were applied across the device in the laboratory measurements. In the experiments, the active electrode was grounded, while the ohmic electrode was connected to the voltage source v_S. Since, as illustrated in plot (b) of the same figure, the theoretical analysis, reported throughout the manuscript, assumes the application of the voltage stimulus V_S to the active electrode, with the ohmic electrode grounded, in the experimental tests, the device undergoes a SET (RESET) resistance switching transition as a positive (negative) voltage v_S is set to fall between its terminals. A scanning electron microscope (SEM) top-view and a transmission electron microscope (TEM) cross-sectional image of a single Pt/TaO_x/Ta/Pt VCM device, occupying a junction area of $3 \times 3\ \mu m^2$ within a passive crossbar array, are, respectively, shown in plots (a) and (b) of Figure 15 (Ascoli et al., 2022).

7.2 Information about the measurement procedure

The setup for the measurement employs a Keithley 4200-SCS parameter analyser, outfitted with ultra-fast pulse measurement units from the 4225-PMU family, as well as with remote preamplifier/switch modules, facilitating the detection of small currents. Figure 16 showcases a photograph of the Cascade Microtech MPS150 probe station, employing a Motic PSM-1000 microscope, and a pair of manually operated DPP220 probe positioners. The Keithley 4200-SCS parameter analyser can generate periodic square-wave voltage signals with amplitudes within the range (−40 V, +40 V), widths reducible down to 70 ns, and rising, as well as falling flanks stretching across a minimum time span of 20 ns each. The same tool allows measuring currents ranging between 100 nA and 200 mA. The operation of the device is orchestrated through a custom Python script, which allows transmitting commands to the experimental apparatus and retrieving measurement data from the sample under test via a general purpose interface bus (GPIB).

To program a specific resistance state into the TaO_x VCM device across the range (10 $k\Omega$, 55 $k\Omega$) ahead of the bistability test, an asymmetric triangular voltage stimulus v_S at frequency 1 kHz, with a fixed positive SET amplitude $\hat{v}_{SET}$ and programmable negative RESET amplitude $\hat{v}_{RESET}$, were preliminarily applied between its terminals, according to the qualitative diagram of Figure 14A. Over each cycle, the device was first subject to the triangular pulse of positive polarity and then to the one of negative polarity. $\hat{v}_{SET}$ was chosen equal to 1.4 V, whereas $\hat{v}_{RESET}$ was stepped across a set of values in the range (−2.2 V, −1.6 V). Figure 17A shows the current i *versus* voltage v locus of the device for 10 consecutive cycles of the periodic triangular stimulus in the scenario, where the RESET input amplitude was adjusted to the highest value in this range, specifically −1.6 V. Removing the stimulus after the 10th cycle, the resistance of the device was found to be equal to 10 kΩ, as read a few minutes after the 10-cycle triangular stimulation by applying a sequence of five read pulses, featuring amplitude 0.1 V, width 1 ms, and 0.1-ms-long rising and falling flanks, and spaced out by 0.01 ms one from the other, sampling 20 times per pulse, at regular time intervals, the current flowing through the device, when the voltage across it was fixed to the given plateau level, and

averaging out the resulting 100 measurements. The application of the same procedure, when 2.2 V was assigned to the modulus of $\hat{v}_{S,RESET}$ [see plot (b) of Figure 17 for the *i versus v* locus of the device over 10 cycles of the triangular voltage stimulus], allowed to write a higher resistance into the ReRAM device, specifically 55 kΩ, as measured, on average, from the 100 data points acquired through the 5-read-pulse sequence. Decreasing the modulus of $\hat{v}_{S,RESET}$ further below 1.6 V, occasionally a resistance lower than 10 kΩ may be written into the device, which, however, behaves in a rather stochastic and unreliable fashion [see Figures 1C, D in (Marchewka et al., 2016)]. Increasing the modulus of $\hat{v}_{S,RESET}$ further above 2.2 V, the device resistance may not be programmed to a higher value. The interested reader is invited to consult Marchewka et al. (2016) and La Torre et al. (2019) for more details on this saturation effect. Stepping $\hat{v}_{RESET}$ to the ith voltage in the set $S_{\hat{v}_{RESET}} \triangleq \{-1.6V, -1.65V, -1.7V, -1.8V, -1.9V, -1.95V, -2V, -2.1V, -2.2V\}$ allowed to set the initial resistance of the ReRAM cell to the ith value in the set $S_{1,R} \triangleq \{10k\Omega, 12\ k\Omega, 20\ k\Omega, 25\ k\Omega, 30\ k\Omega\ 33\ k\Omega, 36\ k\Omega, 45\ k\Omega$, and $55\ k\Omega\}$ for $i \in \{1, 2, 3, 4, 5, 6, 7, 8, 9\}$. For each initial condition in the set $S_{1,R}$, the device sample was then disconnected from the power for a few seconds in preparation for the bistability test. The bistability test for the ith initial condition in this set of cardinality 9 shall be denoted as scenario i in the discussion to follow.

Here, a four-pulse-per-cycle train voltage signal v_S was let to fall across the device for as many as 200 cycles. In each period, the voltage source was regulated in such a way to generate, first, a negative write pulse of amplitude $V_- = -1.1$ V and width $\tau_- = 0.5$ ms; then, after a pause of 0.01 ms, a first read pulse, featuring amplitude 0.1 V, width 1 ms, and 0.1-ms-long rising and falling flanks; subsequently, after another pause of 0.01 ms, a positive write pulse of amplitude $V_+ = +0.7$ V and width $\tau_+ = 0.5$ ms; and finally, after yet another pause of 0.01 ms, a second read of pulse, featuring amplitude 0.1 V, width 1 ms, and 0.1-ms-long rising and falling flanks.

Importantly, as recently reported (Wiefels et al., 2023), a stochastic relaxation phenomenon emerges in the nanodevice under zero input. In particular, ions hop randomly across the powered-off physical stack at ambient temperature. These stochastic effects may result in significant changes in the device resistance over time. In fact, they explain why, for each of a few scenarios from the set of cardinality 9 under consideration, extracting 20 samples of the device current at regular time intervals as the read pulse, directly following the RESET write pulse in the first cycle of the pulse train voltage stimulus, was let to fall across the physical stack, the average resistance of the ReRAM cell was found to be lower than the respective initial condition. This happened for those scenarios indexed through the labels listed in the set {3,4,6,7,8,9}. In fact, with reference to the scenario labelled via the index i, which ranges across the set {1, 2, 3, 4, 5, 6, 7, 8, 9}, right previous to the application of the SET write pulse between its terminals in the first cycle of the pulse train voltage stimulus, the VCM device was found to admit the ith resistance in the set $S_{2,R} \triangleq \{R_{0,1}, R_{0,2}, R_{0,3}, R_{0,4}, R_{0,5}, R_{0,6}, R_{0,7}, R_{0,8}, R_{0,9}\} = \{11.133, 14.623, 15.337, 24.586, 32.920, 26.399, 21.584, 36.571, 32.563\}k\Omega$. For this reason, we discarded the first cycle in the train voltage stimulus v_S, employed in the bistability test, using, however, its second read pulse to define a new initial condition for the VCM device as the average between 20 regularly spaced out measurements. Hence, in the ith scenario, with $i \in \{1, 2, 3, 4, 5, 6, 7, 8, 9\}$, directly before the application of the second sequence of four pulses across its physical stack, the ReRAM cell was found to hold the ith resistance in the set $S_{3,R} \triangleq \{R_{0,1}, R_{0,2}, R_{0,3}, R_{0,4}, R_{0,5}, R_{0,6}, R_{0,7}, R_{0,8}, R_{0,9}\} = \{3.032, 3.456, 4.005, 4.367, 6.459, 5.243, 4.456, 30.861, 37.185\}k\Omega$. Figure 18A shows the initial periods of the time course of the train voltage stimulus except for its first four pulses. The pulse train voltage signal induces the simplest form of local fading memory in the nanodevice, namely, a bistable oscillatory response. In fact, as shown in Figure 18B, under the application of such a periodic excitation for as many as 199 cycles, the device resistance, measured at regular time intervals, 20 times per read pulse, after each write operation over each period, was found to evolve toward one of two possible steady-state oscillatory solutions, depending upon its initial condition. In particular, the traces, associated with the 1st, 2nd, and 3rd and 4th (5th, 6th, 7th, 8th, and 9th) initial conditions from the set $S_{3,R}$, progressively approach the lower (upper) oscillatory solution. It follows that the sets of initial conditions, from which the memristive system respectively asymptotically approaches the lower or the upper oscillatory attractor from the admissible pair, are separated by an initial condition lying between $R_{0,4} = 4.367\ k\Omega$ and $R_{0,7} = 4.456\ k\Omega$. For resistance initial conditions above the separatrix, the device experiences much slower dynamics than otherwise. In fact, despite, as shown through red and purple traces in plot (f) of Figure 19, the experiment was iterated for as many as six iterations for two particular resistance initial conditions from $S_{3,R}$, specifically $R_{0,1} = 3.032\ k\Omega$ and $R_{0,9} = 37.185\ k\Omega$, falling, respectively, in the basin of attraction of the lower and upper oscillatory attractors for the periodically driven memristive system, the application of the four-pulse-per-cycle train voltage stimulus across the physical stack for as many as 1,200 periods was insufficient for transients to vanish for the initial condition above the separatrix, which prevented the observation of the upper steady-state oscillation in the device resistance at the end of the experiment. This notwithstanding, it is the pure existence of the *separatrix* (Strogatz, 2014), which provides firm evidence for the bistability of the periodically forced ReRAM cell.

Since the device sample, employed in the experimental test for bistability, is different from the one, the JART VCM model, used for the system-theoretic analysis reported so far in this paper, was originally (Ascoli et al., 2022) fitted to, a parameter tuning procedure had to be run once again to match qualitatively the behaviour of its solutions to the measurement data from Figures 18B, 19F. A standard optimisation algorithm, massaging a few parameters, specifically $e \cdot \phi_{bn0}$, $R_{th,eff,RESET}$, and $R_{th,eff,SET}$, in such a way to minimise the error between the model predictions and these experimental measurements, resulted in their update, relative to the nominal values in Supplementary Table A1, as listed at the end of Supplementary Appendix A.1 (refer to Supplementary Table A2). In order to simplify the numerical integration of the JART VCM model, the read pulses were omitted from the voltage signal assumed to fall across the memristor. In fact, as shown in Figure 19A, in the numerical simulation, replicating qualitatively the experimental data, v_S was shaped as a two-pulse-per-cycle train voltage stimulus. Taking into account the different approach, employed in the model simulation to apply the voltage stimulus across the ReRAM cell (recall Figure 14B), as compared to what was

performed in the experiment (recall Figure 14A), the first (second) pulse within each T = 1-ms-long period of the input signal v_S is assumed to undergo a RESET (SET) transition in the nanodevice, featuring an amplitude V_+ of +1.1 V (V_- of −0.7 V) and a width τ_+ of 0.5 ms (τ_- of 0.5 ms). Figure 19B shows the $\hat{r}(\bar{x}, V_+, V_-)$ *versus* $\bar{x}$ locus for (V_+, V_-) = (+1.1 V, −0.7 V). The horizontal line r = 1 crosses this locus in three points, $\bar{x}_{eq,1} = 1.000 \cdot 10^{24}$, $\bar{x}_{eq,2} = 2.862 \cdot 10^{25}$, and $\bar{x}_{eq,3} = 2.670 \cdot 10^{27}$, the first and third (second) of which correspond (corresponds) to locally stable (an unstable) equilibria (equilibrium) for the TA-SE (7), as may be evidenced from the graph of $\dot{\bar{x}}$ as a function of $\bar{x}$ for the given input parameter setting (see plot (c) of Figure 19).

Interestingly, the device resistances, computed at the read voltage level V of −0.1 V at the first, second, and third TA-SE equilibria, respectively, read as $R(\bar{x}_{eq,1})$ = 248.792MΩ, $R(\bar{x}_{eq,2})$ = 5.952kΩ, and $R(\bar{x}_{eq,3})$ = 673.901Ω. The SCPM confirms the predictions from the TA-SDR analysis, as illustrated in Figure 19D, which shows that the locally stable (unstable) fixed points (fixed point) of the Poincaré map $x_{k+1} = \mathcal{P}(x_k)$ are located at $x_1^\star = 1.000 \cdot 10^{24}$, and $x_3^\star = 2.675 \cdot 10^{27}$ ($x_2^\star = 3.463 \cdot 10^{25}$). Importantly, the device resistances, computed at the read voltage level V of −0.1 V at the first, second, and third fixed points, respectively, read as $R(x_1^\star)$ = 248.792MΩ, $R(x_2^\star)$ = 4.362kΩ, and $R(x_3^\star)$ = 673.834Ω.

Figure 19E shows the model prediction for the time course of the device resistance from each of the initial conditions, falling in the set S_{R_3}, and evaluated one by one from the state initial conditions at the corresponding positions in the set $S_{3,x} \triangleq \{x_{0,1}, x_{0,2}, x_{0,3}, x_{0,4}, x_{0,5}, x_{0,6}, x_{0,7}, x_{0,8}, x_{0,9}\}$ = {$4.564{\cdot}10^{25}$, $3.673{\cdot}10^{25}$, $3.460{\cdot}10^{25}$, $2.737{\cdot}10^{25}$, $3.081{\cdot}10^{25}$, $3.414{\cdot}10^{25}$, $1.465{\cdot}10^{25}$, $1.383{\cdot}10^{25}$}, assuming the voltage v across the device to be fixed to the DC read level V of −0.1 V.

The separatrix point, appearing at $R(x_2^\star)$, is just 5Ω to the left of the lower bound in the range, where it was found to lie in the experiments. As a result, here only the traces, starting off from the first three initial conditions in $S_{3,R}$, progressively approach the lower oscillatory steady state. The cyan (green) trace in Figure 19F shows how the time waveform of the device resistance, started off at $R_{0,1}$ = 3.032 kΩ ($R_{0,9}$ = 37.185 kΩ), captures the corresponding experimental red (purple) trace, converging toward the lower (upper) steady-state oscillatory solution. The solid cyan trace in plot (g) visualises the device memory state over time, resulting from a numerical integration of the memristor DAE set when the initial condition x_0 is set to the first fixed point $x_1^\star$ of the Poincaré map. Here, the black dashed horizontal line shows the location of the TA-SE equilibrium $\bar{x}_{eq,1}$. Plot (h) is a close-up view of plot (g) around the oscillatory solution for the memory state. The black dash-dotted horizontal line meets the memristor state solution at its maxima of ordinate $x_1^\star$. Figure 19I depicts through a green trace the time waveform of the memory state, as recorded during a numerical simulation of the JART VCM v1 model in the scenario where the initial condition x_0 was set to the third fixed point $x_3^\star$ of the Poincaré map. Last but not least, taking into account the intrinsic variability in the electrical behaviour of the device from sample to sample, according to the adaptation of the JART VCM model from Bengel et al. (2020), it was nevertheless possible to verify, to a certain extent, the robustness in the bistable response of the ReRAM cell under the earlier specified periodic excitation. In particular, as anticipated above, the unstable map fixed point $x_2^\star$, which acts as a separatrix (Strogatz, 2014) between the basins of attraction of the two coexisting locally stable map fixed points $x_1^\star$ and $x_3^\star$, and provides evidence for the bistability of the ReRAM device-based oscillator by virtue of its sole appearance, was found to exist at all times under any possible combination of values, assigned to each of five model parameters of critical impact on the device-to-device variability, specifically r_{fil}, l_{cell}, l_{disc}, x_{min}, and x_{max}, from a set of cardinality 2, including −10% and +10% of the respective nominal value, as indicated in Supplementary Table A1. The blue circles in Figure 19J show the spread in the value of the unstable fixed point $x_2^\star$ of the Poincaré map, expressed in terms of the device resistance as $R(x_2^\star)$, for all the 32 possible combinations of values, assigned to these five parameters, against the filament radius r_{fil}, which was found to hold the stronger correlation with the variable reported along the vertical axis, as may be inferred by comparing the impact that its changes, relative to the nominal level (see the reference circle marker), have on the location of the separatrix point.

8 Conclusion

Typically, the application of a periodic stimulus, from classes commonly used in electrical engineering, including sine-waves, triangular waves, and square waves, to a non-volatile resistance switching memory induces a unique, i.e., initial condition-independent asymptotic oscillatory response in its memory state (Ascoli et al., 2017), a property referred to as fading memory (Boyd and Chua, 1985). On the other hand, local fading memory effects are said to emerge in a system, which, under the effects of some input, may asymptotically exhibit a number of different behaviours, locking into each of the possible operating modes for all initial conditions from the respective basin of attraction (Ascoli et al., 2016a; Ascoli et al., 2016b). A numerical investigation (Ascoli et al., 2022), based upon a predictive model (Hardtdegen et al., 2018; Bengel et al., 2022), recently unveiled the emergence of bistability, i.e., the simplest form of local fading memory, in the oscillatory response of the physical realization of a tantalum oxide ReRAM cell to a particular periodic triangular stimulus. However, the manuscript, reporting this interesting observation, made independently also from other scientists, exploring the non-linear dynamics of a different non-volatile memristor via bifurcation analysis (Pershin and Slipko, 2019), provided no further analysis to elucidate the origin for the coexistence of two stable oscillatory steady states for the nano-device. As another open question, stemming from this research work, it would be of interest to understand how to modulate the properties of the stimulus so as to induce the emergence of bifurcation phenomena, whereby the nature of the fading memory effects, appearing in the device, would switch from local to global or *vice versa*. Investigating whether there exist periodic excitations, inducing more complex forms of local fading memory than bistability in the nano-device, is a follow-up problem worthy of study. A theoretical research work is first presented in this manuscript to provide comprehensive answers to all these questions. In particular, the state dynamic route technique, inspired to the time averaging methodology (Guckenheimer and Holmes, 1983) from the theory of non-linear dynamics, and to the bifurcation study, reported in Pershin and Slipko (2019), is first introduced as extension of

the dynamic route map graphic tool (Chua, 2018), which is applicable to the analysis of first-order systems subject to bias inputs only, for the exploration of the response of systems of this kind to AC periodic square pulse train-based stimuli. Recurring to this technique, a rigorous and systematic strategy is then set up to massage heights and widths of the two square pulses of opposite polarity, composing a periodic pulse train-based input over each cycle, so as to modulate the number and stability properties of the admissible oscillatory steady states of the nano-device. Numerical simulations of the device model in a number of excitation scenarios provide robust proof of evidence for the accuracy of the proposed theoretical framework in predicting all the possible levels, around which the state of the memristor, subject to a periodic two-pulse-per-cycle train stimulus, may be found to revolve, after transients vanish, for a given choice of the four input parameters. Toward the experimental verification of the theory, developed in this research study, the intrinsic physical limitations to the measurement instrumentation tools need to be taken into account for the definition of an *ad hoc* input parameter setting in each case study. In this regard, as shown in Section 6, margins for experimental setup optimization exist, given that the set of bifurcations in number, stability, and kinds of oscillatory solutions for the memory state of the ReRAM cell upon a pulse width ratio sweep varies critically with the pulse height parameter pair selection, which widens considerably the spectrum of opportunities available to the circuit designer[17]. On the basis of these considerations, as reported in Section 7, we were able to devise an opportune experimental setup, through which we confirmed the theoretical predictions on the bistable oscillatory response of the ReRAM cell under suitable periodic pulse train stimulation in the laboratory, as reported at the end of the manuscript. In particular, the experimental analysis, corroborating the accuracy of our theory, allowed identifying the signature for the bistability of the periodically forced nanodevice, namely, the existence of an initial condition for its resistance, separating the basins of attraction of its two admissible oscillatory steady states. *To the best of our knowledge, this is the first time local fading memory effects, resulting in steady-state bistability, are discovered at the nanoscale in a non-volatile resistance switching memory!* Importantly, numerical investigations of the JART VCM model further showed how a separatrix point keeps existing across the allowable domain for the ReRAM cell resistance even under non-negligible device-to-device variability effects. Moreover, as described in Supplementary Appendix A.2, the application of the system-theoretic framework, presented in this paper, under the additional constraint, allowing the SET and RESET pulse widths to differ by three orders of magnitude at most, enables determining an appropriate input parameter quartet for the execution of a practical tristability test on the oscillatory device in the laboratory. The theoretical prediction of the coexistence of more than two oscillatory steady states in the nanodevice for suitable periodic excitations awaits now for experimental verification. Moreover, toward a future exploitation of these peculiar nonlinear phenomena for electronics applications, one of the tasks to fulfil involves the inclusion of non-idealities, especially those factors responsible for stochastic cycle-to-cycle electrical behavioural variability, in the ReRAM cell model to understand how they affect the shape of the $\hat{r}(\bar{x}, V_+, V_-)$ *versus* $\bar{x}$ locus under pulse height pair modulation during the device lifetime, toward the identification of an *ad hoc* operating region of the V_+–V_- parameter domain, where, for any given case study of interest, the oscillatory mode, emerging under a suitable pulse width ratio choice, is most robust against these unwanted effects. The peculiar capability of the non-volatile memristor physical realization, under the zooming lens in this manuscript, to feature alternatively a local or global form of fading memory, depending upon the periodic stimulus, may inspire the design of innovative energy-efficient sensing and mem-processing circuits and systems for edge computing and Internet-of-Things applications in the years to come. The research methodologies, presented in this work, are applicable upon suitable adaptation also to other non-volatile resistance switching memories (Ascoli et al., 2024) and to the class of volatile memristor devices (Messaris et al., 2024). Importantly, they shed light into the fundamental role that non-linear circuit and system theory (Corinto et al., 2021) assumes for unlocking the full potential of intrinsically nonlinear memristive devices in the electronics of the future (Goswami et al., 2021).

17 It is worth pinpointing that the rich oscillatory dynamics, reported in this manuscript, was induced in the ReRAM cell via a simple square wave stimulus, including just two pulses per cycle. Adding more pulses within the input period is expected to increase the complexity of the dynamical phenomena emerging consequently across the device physical medium.

Data availability statement

The raw data supporting the conclusion of this article will be made available by the authors, without undue reservation.

Author contributions

NS: conceptualization, data curation, formal analysis, investigation, methodology, validation, and writing–review and editing. AA: conceptualization, data curation, formal analysis, investigation, methodology, supervision, validation, visualization, writing–original draft, and writing–review and editing. IM: investigation and writing–review and editing. ASD: investigation and writing–review and editing. SM: investigation and writing–review and editing. VR: investigation and writing–review and editing. RT: formal analysis, validation, and writing–review and editing. LC: formal analysis, validation, and writing–review and editing.

Funding

The author(s) declare that financial support was received for the research, authorship, and/or publication of this article. LC is

supported in part by the United States Air Force Office of Scientific Research (AFOSR) grant number FA 9550-18-1-0016. The Deutsche Forschungsgemeinschaft is also acknowledged for the financial support to the project "Universal Memcomputing in Hardware Realizations of Memristor Cellular Nonlinear Networks" (project number: 441957207).

Acknowledgments

The authors are thankful to Sitandi Zhang (Forschungszentrum Jülich) for performing the experiments, discussed in Section 7, which allowed validating the theory developed in this scientific study. They are also grateful to Prof. Marco Gilli (Politecnico di Torino) and Prof. Fernando Corinto (Politecnico di Torino) for their precious contributions in the theoretical analysis of the bistability of the periodically forced ReRAM cell from Forschungszentrum Jülich over the entire course of this research work. They also extend their gratitude to Vasilis Ntinas (Technische Universität Dresden) and Dimitris Prousalis (Technische Universität Dresden) for contributing to the numerical investigations, allowing to refit the JART VCM v1 model to the experimental data and to verify the robustness of the bistability of the device against its intrinsic cycle-to-cycle variability. Last but not least, Tim Kempen (Forschungszentrum Jülich) is sincerely acknowledged for the provision of insightful recommendations for the numerical investigations, reported in Supplementary Appendix A.2, devoted to the identification of a suitable parameter setting for a periodic square wave voltage stimulus, allowing, as next step of our research, the pursuit of an experimental tristability test on the oscillatory ReRAM cell, taking into account the physical limitation of the pulse generators available at our laboratories.

Conflict of interest

The authors declare that the research was conducted in the absence of any commercial or financial relationships that could be construed as a potential conflict of interest.

The handling editor CR declared a past co-authorship with the author AA.

Publisher's note

Supplementary material

The Supplementary Material for this article can be found online at: https://www.frontiersin.org/articles/10.3389/fnano.2024.1301320/full#supplementary-material

References

Ascoli, A., Menzel, S., Rana, V., Kempen, T., Messaris, I., Demirkol, A. S., et al. (2022). A deep study of resistance switching phenomena in TaOx ReRAM cells: system-theoretic dynamic Route map analysis and experimental verification. *Adv. Electron. Mater.* 8 (8), 2200182. doi:10.1002/aelm.202200182

Ascoli, A., Schmitt, N., Messaris, I., Demirkol, A. S., Strachan, J. P., Tetzlaff, R., et al. (2024). An analytical approach to engineer multistability in the oscillatory response of a pulse-driven ReRAM. *Sci. Rep.* 14 (5626), 5626. doi:10.1038/s41598-024-55255-7

Ascoli, A., Schmitt, N., Messaris, I., Demirkol, A. S., Tetzlaff, R., and Chua, L. O. (2023b). The State Change Per Cycle Map: a novel system-theoretic analysis tool for periodically driven ReRAM cells. *Front. Electron. Mater.* 23, 32. doi:10.3389/femat.2023.1228899

Ascoli, A., Schmitt, N., Messaris, I., Demirkol, A. S., Tetzlaff, R., Strachan, J. P., et al. (2023a). "Local fading memory effects in a tantalum oxide ReRAM cell from Hewlett packard labs," in Proceedings of the IEEE Int. Conference on Metrology for Extended Reality, Artificial Intelligence and Neural Engineering (MetroXRAINE), Milano, Italy, October 25-27, 2023 (IEEE).

Ascoli, A., Tetzlaff, R., and Chua, L. O. (2016a). The first ever real bistable memristors–Part I: theoretical insights on local fading memory. *IEEE Trans. Circuits Systems–II Express Briefs* 63 (12), 1091–1095. doi:10.1109/tcsii.2016.2604567

Ascoli, A., Tetzlaff, R., and Chua, L. O. (2016b). The first ever real bistable memristors–Part II: design and analysis of a local fading memory system. *IEEE Trans. Circuits Systems–II Express Briefs* 63 (12), 1096–1100. doi:10.1109/tcsii.2016.2613560

Ascoli, A., Tetzlaff, R., Chua, L. O., Strachan, J. P., and Williams, R. S. (2016c). History erase effect in a non-volatile memristor. *IEEE Trans. Circuits Systems–I (TCAS–I) Regul. Pap.* 63 (3), 389–400. doi:10.1109/tcsi.2016.2525043

Ascoli, A., Tetzlaff, R., Chua, L. O., Strachan, J. P., and Williams, R. S. (2017). "Memory loss in a tantalum oxide memristor," in Pages 94–101 of: Advances in Science and Technology, Proc. Int. Conference on Smart Materials, Structures and Systems (Perugia, Italy, 5-9 June 2016), vol. 99, Perugia, Italy, 5-9 June 2016 (Switzerland: Trans Tech Publications).

Ascoli, A., Tetzlaff, R., and Menzel, S. (2018). Exploring the dynamics of real-world memristors on the basis of circuit theoretic model predictions. *IEEE Circuits Syst. Mag.* 18 (2), 48–76. doi:10.1109/mcas.2018.2821760

Bengel, C., Siemon, A., Cüppers, F., Hoffmann-Eifert, S., Hardtdegen, A., von Witzleben, M., et al. (2020). Variability-aware modeling of filamentary oxide-based bipolar resistive switching cells using SPICE level compact models. *IEEE Trans. Circuits Systems–I Regul. Pap.* 67 (12), 4618–4630. doi:10.1109/tcsi.2020.3018502

Bengel, C., Zhang, D. K., Waser, R., and Menzel, S. (2022). JART VCM v1 verilog-A compact model user guide. Available at: https://www.emrl.de/JART-files/User_Guide_for_the_JART_VCM_v1_Compact_Model.pdf.

Boyd, S., and Chua, L. O. (1985). Fading memory and the problem of approximating nonlinear operators with Volterra series. *IEEE Trans. Circuits Syst.* 32 (11), 1150–1161. doi:10.1109/tcs.1985.1085649

Buckwell, M., Ng, W. H., Mannion, D. J., Cox, H. R. J., Hudziak, S., Mehonic, A., et al. (2021). Neuromorphic dynamics at the nanoscale in silicon suboxide RRAM. *Front. Nanotechnol.* 3 (699037), 10. doi:10.3389/fnano.2021.699037

Chua, L. O. (2018). Five non-volatile memristor enigmas solved. *Appl. Phys. A* 124 (563), 563. doi:10.1007/s00339-018-1971-0

Corinto, F., Civalleri, P. P., and Chua, L. O. (2015). A theoretical approach to memristor devices. *IEEE J. Emerg. Sel. Top. Circuits Syst. (JETCAS)* 5 (2), 123–132. doi:10.1109/jetcas.2015.2426494

Corinto, F., Forti, M., and Chua, L. (2021) *Nonlinear circuits and systems with memristors: nonlinear dynamics and analogue computing via the flux-charge analysis method*. 1. Cham: Springer.

Di Ventra, M., and Traversa, F. L. (2018). Perspective: memcomputing: Leveraging memory and physics to compute efficiently. *J. Appl. Phys.* 123 (180901), 15. doi:10.1063/1.5026506

Goswami, S., Pramanick, R., Patra, A., Rath, S. P., Foltin, M., Ariando, A., et al. (2021). Decision trees within a molecular memristor. *Nature* 597 (7874), 51–56. doi:10.1038/s41586-021-03748-0

Guckenheimer, J., and Holmes, P. (1983) *Nonlinear oscillations, dynamical systems, and bifurcations of vector fields*. 1. New York, USA: Springer-Verlag New York, Inc.

Hardtdegen, A., La Torre, C., Cüppers, F., Menzel, S., Waser, R., and Hoffmann-Eifert, S. (2018). Improved switching stability and the effect of an internal series resistor in HfO_2/TiO_x bilayer ReRAM cells. *IEEE Trans. Electron Devices* 65 (8), 3229–3236. doi:10.1109/ted.2018.2849872

Hu, M., Strachan, J. P., Li, Z., Grafals, E. M., Davila, N., Graves, C., et al. (2016). "Dot-product engine for neuromorphic computing: programming 1T1M crossbar to accelerate matrix-vector multiplication," in Proceedings of the Design Automation Conference (DAC), Austin Texas, June 5 - 9, 2016.

Ielmini, D., and Waser, R. (2016) *Resistive switching: from fundamentals of nanoionic redox processes to memristive device applications*. 1. Wiley-VCH Verlag GmbH & Co. KGaA.

La Torre, C., Zurhelle, A. F., and Menzel, S. (2019). "Compact modelling of resistive switching devices based on the valence change mechanism," in Proc. of the Int. Conf. on Simulation of Semiconductor Processes and Devices (SISPAD), Udine, Italy, 4-6 September 2019.

Lenk, C., Hövel, P., Ved, K., Durstewitz, S., Meurer, T., Fritsch, T., et al. (2023). Neuromorphic acoustic sensing using an adaptive microelectromechanical cochlea with integrated feedback. *Nat. Electron.* 6, 370–380. doi:10.1038/s41928-023-00957-5

Li, C., Hu, M., Li, Y., Jiang, H., Ge, N., Montgomery, E., et al. (2018). Analogue signal and image processing with large memristor crossbars. *Nat. Electron.* 1 (1), 52–59. doi:10.1038/s41928-017-0002-z

Marchewka, A., Roesgen, B., Skaja, K., Du, H., Jia, C.-L., Mayer, J., et al. (2016). Nanoionic resistive switching memories: on the physical nature of the dynamic reset process. *Adv. Electron. Mater.* 2 (1), 1500233. doi:10.1002/aelm.201500233

Menzel, S., Waser, R., Siemon, A., La Torre, C., Schulten, M., Ascoli, A., et al. (2017). "On the origin of the fading memory effect in ReRAMs," in Proc. of the Int. Symp. On Power and Timing, Modeling, Optimization, and Simulation (PATMOS), Thessaloniki, Greece, September 25-27, 2017 (IEEE).

Messaris, I., Ascoli, A., Demirkol, A. S., Ntinas, V., Prousalis, D., and Tetzlaff, R. (2024). High frequency response of volatile memristors. *Adv. Electron. Mater*. doi:10.1002/aelm.202400172

Messaris, I., Ascoli, A., Demirkol, A. S., and Tetzlaff, R. (2023). High frequency response of non-volatile memristors. *IEEE Trans. Circuits Systems-I (TCAS-I) Regul. Pap.* 70 (2), 566–578. doi:10.1109/tcsi.2022.3219368

Mikolajick, T., Salinga, M., Kund, M., and Kever, T. (2009). Nonvolatile memory concepts based on resistive switching in inorganic materials. *Adv. Eng. Mater.* 11 (4), 235–240. doi:10.1002/adem.200800294

Milano, G., Pedretti, G., Montano, K., Ricci, S., Hashemkhani, S., Boarino, L., et al. (2022). In materia reservoir computing with a fully memristive architecture based on self-organizing nanowire networks. *Nat. Mater.* 21 (2), 195–202. doi:10.1038/s41563-021-01099-9

Ntinas, V., Ascoli, A., Messaris, I., Wang, Y., Rana, V., Menzel, S., et al. (2022). Toward simplified physics-based memristor modeling of valence change mechanism devices. *IEEE Trans. Circuits Systems-II (TCAS-II) Express Briefs* 69 (5), 2473–2477. doi:10.1109/tcsii.2022.3160304

Ntinas, V., Patel, D., Wang, Y., Messaris, I., Rana, V., Menzel, S., et al. (2023). "A simplified variability-aware VCM memristor model for efficient circuit simulation," in International Conference on Synthesis, Modeling, Analysis and Simulation Methods, and Applications to Circuit Design, Funchal, Portugal, 3-5 July 2023 (IEEE).

Pershin, Y. V., and Slipko, V. A. (2019). Bifurcation analysis of a TaO memristor model. *J. Phys. D Appl. Phys.* 52 (50), 505304. doi:10.1088/1361-6463/ab4537

Rao, M., Tang, H., Wu, J., Song, W., Zhang, M., Yin, W., et al. (2023). Thousands of conductance levels in memristors integrated on CMOS. *Nature* 615 (7954), 823–829. doi:10.1038/s41586-023-05759-5

Schmitt, N., Ascoli, A., Messaris, I., Demirkol, A. S., Ntinas, V., Prousalis, D., et al. (2023). "Exploration of bistable oscillatory dynamics in a memristor from Forschungszentrum Jülich," in Proceedings of the International Conference on Modern Circuits and Systems Technologies (MOCAST) on Electronics and Communications, Sofia, Bulgaria, 26-28 June 2024 (IEEE).

Sebastian, A., Tuma, T., Papandreou, N., Le Gallo, M., Kull, L., Parnell, T., et al. (2017). Temporal correlation detection using computational phase-change memory. *Nat. Commun.* 8 (1115), 1–10. doi:10.1038/s41467-017-01481-9

Shamsi, J., Avedillo, M. J., Linares-Barranco, B., and Serrano-Gotarredona, T. (2021). Hardware implementation of differential oscillatory neural networks using VO_2-based oscillators and memristor-bridge circuits. *Front. Neurosci.* 15 (674567), 674567. doi:10.3389/fnins.2021.674567

Strachan, J. P., Torrezan, A. C., Miao, F., Pickett, M. D., Yang, J. J., Yi, W., et al. (2013). State dynamics and modeling of Tantalum oxide memristors. *IEEE Trans. Electron Devices* 60 (7), 2194–2202. doi:10.1109/ted.2013.2264476

Strogatz, S. H. (2014) *Nonlinear dynamics and chaos: with applications to physics, biology, chemistry, and engineering (studies in nonlinearity)*. 2. Boulder, Colorado, United States: Westview Press.

Sze, S. M., and Ng, K. K. (2007) *Physics of semiconductor devices*. 3. Hoboken, New Jersey: John Wiley & Sons, Inc.

Talati, N., Gupta, S., Mane, P., and Kvatinsky, S. (2016). Logic design within memristive memories using memristor aided loGIC (MAGIC). *IEEE Trans. Nanotechnol.* 15 (4), 635–650. doi:10.1109/tnano.2016.2570248

Tzouvadaki, I., Gkoupidenis, P., Vassanelli, S., Wang, S., and Prodromakis, T. (2023). Interfacing biology and electronics with memristive materials. *Adv. Mater.* 35 (32), 2210035. doi:10.1002/adma.202210035

Valov, I., Linn, E., Tappertzhofen, S., Schmelzer, S., van den Hurk, J., Lentz, F., et al. (2013). Nanobatteries in redox-based resistive switches require extension of memristor theory. *Nat. Commun.* 4 (1771), 1771. doi:10.1038/ncomms2784

Vontobel, P. O., Robinett, W., Kuekes, P. J., Stewart, D. R., Straznicky, J., and Williams, R. S. (2009). Writing to and reading from a nano-scale crossbar memory based on memristors. *Nanotechnology* 20 (425204), 425204. doi:10.1088/0957-4484/20/42/425204

Wang, Z., Joshi, S., Savel'ev, S. E., Jiang, H., Midya, R., Lin, P., et al. (2017). Memristors with diffusive dynamics as synaptic emulators for neuromorphic computing. *Nat. Mater.* 16 (1), 101–108. doi:10.1038/nmat4756

Waser, R., and Aono, M. (2007). Nanoionics-based resistive switching memories. *Nat. Mater.* 6 (11), 833–840. doi:10.1038/nmat2023

Wiefels, S., Kopperberg, N., Hofmann, K., Otterstedt, J., Wouters, D., Waser, R., et al. (2023). Reliability aspects of 28 nm BEOL-integrated resistive switching random access memory. *Phys. Status Solidi A* 2300401, 13. doi:10.1002/pssa.202300401

Xia, Q., and Yang, J. J. (2019). Memristive crossbar arrays for brain-inspired computing. *Nat. Mater.* 18 (4), 309–323. doi:10.1038/s41563-019-0291-x

Yi, S.-in, Talin, A. A., Marinella, M. J., and Williams, R. S. (2022). Physical compact model for three-terminal SONOS synaptic circuit element. *Adv. Intell. Syst.* 4 (9), 2200070. doi:10.1002/aisy.202270044

Zidan, M. A., Strachan, J. P., and Lu, W. D. (2018). The future of electronics based on memristive systems. *Nat. Electron.* 1 (1), 22–29. doi:10.1038/s41928-017-0006-8